

# CFD ANALYSIS OF THE INFLUENCE OF CONTRACTION SIZE ON ELECTROVISCOUS FLOW THROUGH THE SLIT-TYPE NON-UNIFORM MICROFLUIDIC DEVICE

Jitendra Dhakar<sup>a</sup>, Ram Prakash Bharti<sup>a,\*</sup>

<sup>a</sup>*Complex Fluid Dynamics and Microfluidics (CFDM) Lab, Department of Chemical Engineering, Indian Institute of Technology Roorkee, Roorkee - 247667, Uttarakhand, INDIA*

---

## Abstract

The electroviscous effects are relevant in controlling and manipulating the fluid, thermal, and mass transport microfluidic processes. The existing research has mainly focused on the fixed contraction ratio ( $d_c$ , i.e., the area ratio of contraction to expansion) concerning the widely used contraction-expansion geometrical arrangement. This study has explored the influence of the contraction ratio ( $d_c$ ) on the electroviscous flow of electrolyte liquids through the charged non-uniform microfluidic device. The numerical solution of the mathematical model (Poisson's, Nernst-Planck, and Navier-Stokes) using a finite element method (FEM) yields the local flow fields. In general, the contraction ratio significantly affects the hydrodynamic characteristics of microfluidic devices. The total electrical potential and pressure drop maximally increase by 1785% and 2300%, respectively, with an overall contraction ratio ( $0.25 \leq d_c \leq 1$ ). Further, an electroviscous correction factor ( $Y$ , i.e., the ratio of apparent to physical viscosity) maximally enhances by 11.24% (at  $K = 8$ ,  $S = 16$  for  $0.25 \leq d_c \leq 1$ ), 31.80% (at  $S = 16$ ,  $d_c = 0.75$  for  $2 \leq K \leq 20$ ), 22.89% (at  $K = 2$ ,  $d_c = 0.5$  for  $4 \leq S \leq 16$ ), and 46.99% (at  $K = 2$ ,  $d_c = 0.75$  for  $0 \leq S \leq 16$ ). The present numerical results may provide valuable guidelines for the performance optimization and design of reliable and essential microfluidic devices.

**Keywords:** Electrolyte liquid, Microfluidic device, Contraction ratio, Pressure-driven flow, Pressure drop, Electroviscous effect

---

\* *Corresponding author.*

*Email address:* rpbharti@iitr.ac.in (Ram Prakash Bharti)

## 1. INTRODUCTION

Due to the rapid development of Lab-on-chip (LOC) devices, microscale channels are widely used in various engineering and biomedical applications, such as DNA analysis [1–3], drug delivery [4, 5], medical diagnosis sensors [6, 7], micro heat exchangers [8–11], and electronic chip cooling [12–15]. In particular, LOC devices are a very efficient way to transport, manipulate and control the flow of electrolyte liquids. Therefore, understanding the fluid dynamics of microscale geometries is essential due to their inherent characteristics, such as the effects of the surface forces (i.e., electroviscous, electromagnetic, surface tension forces, etc.), which are either absent or non-dominant in conventional macroscale geometries. Among others, electroviscous (EV) effects are quite common in electrolyte flow through microdevices due to the induced electric field intensely manipulating the fluid dynamics.

Electroviscous (EV) effects arise due to an interaction of electrolyte liquid with the charged walls of the microfluidic device in the pressure-driven flow (PDF). The charged surfaces attract the counter-ions (and repel co-ions) and, thus, form an ‘electrical double layer’ (EDL), consisting of compact and diffuse layers, in close vicinity of the surface [16, 17]. The convection flow of excess ions in EDL develops a ‘streaming current’ ( $I_s$ ), and the corresponding potential is termed the ‘streaming potential’ (Fig. 1). Subsequently, a ‘conduction current’ ( $I_c$ ), generates the opposite of the pressure-driven flow (PDF) and contributes as an additional hydrodynamic resistance. It results in the retarding of the net flow of liquid in the direction of the primary PDF due to the commonly called ‘electroviscous effect’ [16, 18–20].

Further, non-uniform geometries (e.g., contraction, contraction-expansion,

converging-diverging, X- Y-, T-junctions, and other branching) are commonly used components in the fabrication of the microfluidic devices [18]. In contraction-expansion geometries, additional (i.e., excess) pressure drop resulting from the sudden contraction/expansion enhances the overall pressure drop in the microfluidic devices [18, 20–27]. The contraction ratio ( $d_c$ ) plays a vital role in the hydrodynamics of microfluidic systems and, in general, is defined as follows.

$$d_c = \frac{A_c}{A}, \quad 0 < d_c \leq 1 \quad (1)$$

where,  $A_c$  and  $A$  are the cross-sectional area of contraction and uniform expansion, respectively.

The existing literature concerning electroviscous flow (EVF) in microfluidic devices has been reviewed in our recent studies [20, 26, 27], and thus not repeated here. A voluminous literature has explored various aspects of the electroviscous (EV) effects in the pressure-driven flow (PDF) through charged uniform ( $d_c = 1$ ) microfluidic devices like slit [28–50], rectangular [17, 51, 52], elliptical [53], and cylinder [23, 54–58]. On the other hand, few studies have understood the electroviscous effects by measuring the pressure drop in the non-uniform (contraction-expansion) geometries for a fixed contraction size ( $d_c = 0.25$ ,  $L_c = L_u = L_d$ ) for contraction-expansion slit [18, 20, 26, 27, 59], cylinder [22, 25], and rectangular [24] geometries. Broadly, these studies [18, 20, 22–27] have shown that surface charge density ( $4 \leq S$  or  $S_t \leq 16$ ), surface charge asymmetry ( $S_r = S_b/S_t$ ,  $0 \leq S_r \leq 2$ ), inverse Debye length ( $2 \leq K \leq 20$ ), and slip length ( $0 \leq B_0 \leq 0.20$ ) have remarkably affected the flow characteristics in microfluidic devices at a fixed volumetric flow rate ( $Q$ ). Subsequently, they

[18, 20, 22–27] have presented predictive models for pressure drop, and electroviscous correction factor ( $Y = \Delta P / \Delta P_0$ , where subscript ‘0’ indicates an absence of electrical influences) by accounting the pressure drop in uniform planer channel/pipe by Poiseuille flow, and excess pressure drop due to sudden contraction/expansion under creeping flow. These analytical models maximally overestimated the pressure drop  $\pm 5\%$  compared to their numerical results.

In summary, the literature comprises knowledge of the electroviscous effects in liquid flow through uniform ( $d_c = 1$ ) or non-uniform ( $d_c = 0.25$ ) geometries. While the non-uniform geometries have shown significant influence on the pressure drop and electroviscous effects, the impact of the contraction ratio variation ( $d_c$ ) on the electroviscous flow through charged non-uniform microfluidic devices has been unexplored in the literature, to the best of our knowledge. Hence, the present work aims to numerically investigate the influence of the contraction ratio ( $d_c$ ) on the electrolyte liquid flow through charged non-uniform slit microfluidic devices. A finite element method (FEM) is used to solve the governing equations such as Poisson’s, Nernst-Planck, and Navier-Stokes equations to obtain the flow fields like total potential ( $U$ ), excess ionic charge ( $n_{\pm}$ ), induced electric field strength ( $E_x$ ), velocity ( $\mathbf{V}$ ), and pressure ( $P$ ), for the broader ranges of dimensionless parameters ( $2 \leq K \leq 20$ ,  $4 \leq S \leq 16$ ,  $0.25 \leq d_c \leq 1$ ). Finally, a pseudo-analytical model is developed to estimate the pressure drop ( $\Delta P$ ) and electroviscous correction factor ( $Y$ ) for broader ranges of governing parameters ( $K, S, d_c$ ).

## 2. PROBLEM STATEMENT

Fig. 1 displays the pressure-driven flow of electrolyte liquid through a non-uniform (i.e., contraction-expansion) slit microfluidic device. The two-dimensional (2-D) flow is laminar and fully-developed with an average inflow velocity of  $\bar{V}$  m/s, and the channel walls are uniformly charged with positive charge density ( $\sigma$ , C/m<sup>2</sup>). The contraction section is situated between the upstream and downstream sections in the microchannel. The geometrical characteristics (length, width in  $\mu\text{m}$ ) of upstream, contraction, and downstream sections of the microfluidic device are  $(L_u, 2W)$ ,  $(L_c, 2W_c)$ , and  $(L_d, 2W)$ , respectively; thus, the total length of the microfluidic device is  $L$  ( $= L_u + L_c + L_d$ ), and the contraction ratio is  $d_c$  (Eq. 1). The subscripts ‘u’, ‘c’, and ‘d’ represent the upstream, contraction, and downstream.

The liquid electrolyte is Newtonian (viscosity,  $\mu$  Pa.s), incompressible (density,  $\rho$  kg/m<sup>3</sup>), symmetric (i.e., equal cations and anions,  $n_+ = n_-$  or 1:1) with equal ionic valences ( $z_+ = -z_- = z$ ) and diffusivity ( $\mathcal{D}_+ = \mathcal{D}_- = \mathcal{D}$ , m<sup>2</sup>/s). The bulk (i.e., geometric mean) ionic

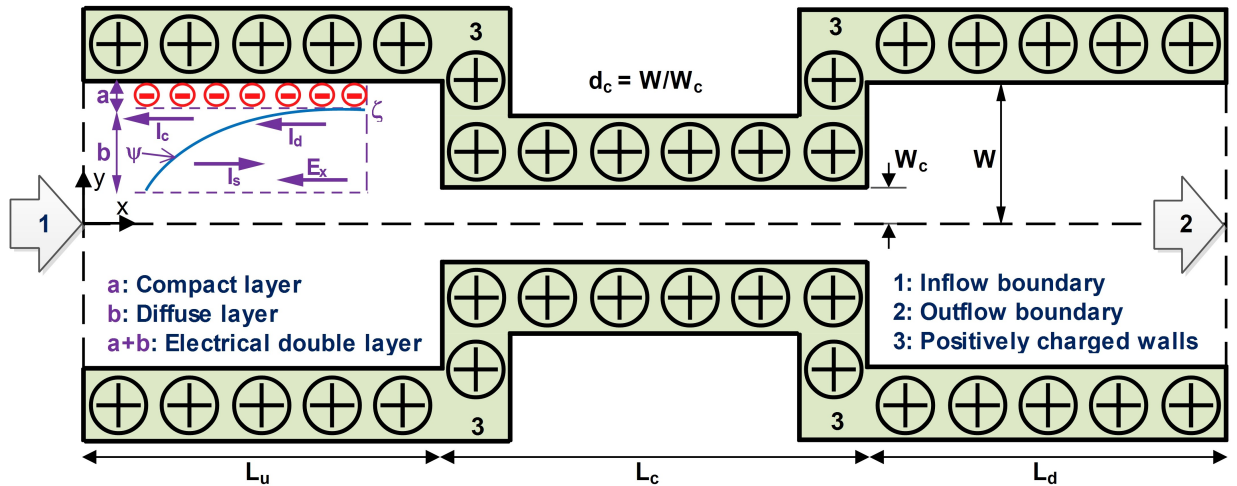


Figure 1: Schematics of pressure-driven flow of liquid electrolyte through charged non-uniform slit microfluidic device.

concentration [60, 61] of liquid is  $n_0 \text{ m}^{-3}$ . The dielectric constant of liquid ( $\varepsilon_r$ ) is spatially constant, and that of the wall is considerably small than liquid ( $\varepsilon_{r,w} \ll \varepsilon_r$ ).

## 2.1. Governing Equations and Boundary Conditions

The above-stated physical problem of electrolyte flow through the charged microfluidic device is, mathematically, governed by Poisson's, Nernst-Planck (N-P), and Navier-Stokes (N-S) equations. The dimensional form of the governing differential equations and boundary conditions are presented in the literature [20], and thus, not repeated here. The mathematical equations [20] are non-dimensionalized using the scaling factors such as  $\bar{V}$ ,  $W$ ,  $n_0$ ,  $W/\bar{V}$ ,  $U_c (= k_B T / ze)$  for velocity, length, the number density of ions, time, and electrical potential, respectively. The dimensionless groups (Reynolds number  $Re$ , Schmidt number  $Sc$ , Peclet number  $Pe$ , inverse Debye length  $K$ , liquid parameter  $\beta$ , surface charge density  $S$ ) obtained from scaling analysis of governing equations and boundary conditions are expressed as follows.

$$Re = \frac{\rho \bar{V} W}{\mu}; \quad Sc = \frac{\mu}{\rho D}; \quad Pe = Re \times Sc; \quad \beta = \frac{\rho \varepsilon_0 \varepsilon_r U_c^2}{2\mu^2}; \quad K^2 = \frac{2W^2 z e n_0}{\varepsilon_0 \varepsilon_r U_c}; \quad S = \frac{\sigma W}{\varepsilon_0 \varepsilon_r U_c} \quad (2)$$

where, the permittivity of free space ( $\varepsilon_0$ , F/m), Boltzmann constant ( $k_B = 1.380649 \times 10^{-23}$  J/K), temperature ( $T$ , K), elementary charge ( $e = 1.602176634 \times 10^{-19}$  C), respectively.

Hereafter, all the variables, fields, and equations are expressed in the dimensionless form.

The Poisson's (Eq. 3), Nernst-Planck (Eq. 4), and Navier-Stokes (Eqs. 5 - 6) equations, in

dimensionless form, are written as follows.

$$\nabla^2 U = -\frac{1}{2} K^2 n^* \quad (3)$$

$$\left[ \frac{\partial n_j}{\partial t} + \nabla \cdot (\mathbf{V} n_j) \right] = Pe^{-1} [\nabla^2 n_j \pm \nabla \cdot (n_j \nabla U)] \quad (4)$$

$$\left[ \frac{\partial \mathbf{V}}{\partial t} + \nabla \cdot (\mathbf{V} \mathbf{V}) \right] = -\nabla P + Re^{-1} \nabla \cdot [\nabla \mathbf{V} + (\nabla \mathbf{V})^T] - \underbrace{(\beta K^2 Re^{-2}) n^* \nabla U}_{\mathbf{F}_e} \quad (5)$$

$$\nabla \cdot \mathbf{V} = 0 \quad (6)$$

where  $\mathbf{V}$ ,  $P$ ,  $n_j$ ,  $n^*(= n_+ - n_-)$ , and  $\mathbf{F}_e$  are velocity vector, pressure, number density of  $j^{th}$  ion, excess charge, and electrical body force, respectively. The total electrical potential ( $U$ ) is the sum of EDL potential ( $\psi$ ) and streaming potential ( $\phi = \phi_0 - x E_x$ ) in the electroviscous flows (EVFs), i.e.,

$$U(x, y) = \phi(x) + \psi(y) \quad (7)$$

where  $\phi_0$  and  $E_x$  are the reference potential at the inlet ( $x = 0$ ), and axially induced electric field strength, respectively. Notably, two potentials ( $\phi$  and  $\psi$ ) act independently as the field directions throughout remain the same for the uniform ( $d_c = 1$ ) geometries. They, however, are strongly coupled for the non-uniform ( $d_c \neq 1$ ) geometries, and the total potential ( $U$ ) is thus computed and analyzed [18, 20, 22, 23, 27].

The governing equations (Eqs. 3 to 6) are subjected to the following relevant dimensionless boundary conditions:

(i) The fully developed velocity ( $\mathbf{V}$ ) and ionic concentration ( $n_{\pm}$ ) fields obtained numerically/analytically [18, 20], and uniform axial potential gradient ( $\partial_x U$ ) are imposed at the

inlet ( $x = 0$ ) boundary as follows.

$$V_x = V_0(y), \quad V_y = 0, \quad n_{\pm} = \exp[\mp\psi_0(y)], \quad \frac{\partial U}{\partial x} = C_1 \quad (8)$$

where  $V_0$  and  $\psi_0$  are the fully developed velocity and EDL potential fields for uniform slit. The constant ( $C_1$ ) is obtained by satisfying the ‘‘current continuity condition’’ (i.e., net current,  $I_{\text{net}} = \nabla \cdot I = 0$ , Eq. 9) expressed [18, 20, 22, 23] as follows.

$$I_{\text{net}} = \underbrace{\int_{-1}^1 n^* \mathbf{V} dy}_{I_s} + \underbrace{\int_{-1}^1 -Pe^{-1} \left[ \frac{\partial n_+}{\partial x} - \frac{\partial n_-}{\partial x} \right] dy}_{I_d} + \underbrace{\int_{-1}^1 -Pe^{-1} \left[ (n_+ + n_-) \frac{\partial U}{\partial x} \right] dy}_{I_c} = 0 \quad (9)$$

where  $I_c$ ,  $I_d$ , and  $I_s$  are the conduction, diffusion and streaming currents, respectively. The diffusion current is zero ( $I_d = 0$ ) at the steady-state condition.

(ii) Both flow and ionic concentration fields are allowed to be fully developed, and uniform axial potential gradient ( $\partial_x U$ ) is maintained at the outlet ( $x = L$ ) boundary open to ambient as follows.

$$\frac{\partial \mathbf{V}}{\partial x} = 0, \quad P = 0, \quad \frac{\partial n_j}{\partial x} = 0, \quad \frac{\partial U}{\partial x} = C_2 \quad (10)$$

The constant ( $C_2$ ) is obtained by satisfying Eq. (9) at the outlet ( $x = L$ ) boundary.

(iii) No-slip, solid, impermeable walls of the device are uniformly charged, i.e.,

$$\mathbf{V} = 0, \quad \mathbf{f}_j \cdot \mathbf{n}_b = 0, \quad (\nabla U \cdot \mathbf{n}_b) = S \quad (11)$$

where  $\mathbf{f}_j$  is the flux density of ions described by Einstein relation [20, 62], and  $\mathbf{n}_b$  is unit vector normal to the boundary.

The coupled mathematical model (Eqs. 3 to 11) has been numerically solved to obtain the flow



fields, i.e., total potential ( $U$ ), ionic concentration ( $n_{\pm}$ ), velocity ( $\mathbf{V}$ ), pressure ( $P$ ), excess charge ( $n^*$ ), and induced electric field strength ( $d_x$ ) fields, in the non-uniform microfluidic device for wide ranges of dimensionless parameters ( $2 \leq K \leq 20$ ,  $4 \leq S \leq 16$ ,  $0.25 \leq d_c \leq 1$ ).

At this point, it is appropriate to briefly discuss the important quantities and definitions used in the subsequent discussion of the new results. For instance, in order to explore the influence of the contraction ratio ( $d_c$ ), the hydrodynamic quantities (say,  $\lambda$ ) have been normalized, under otherwise identical conditions, as follows.

$$\lambda_n = \left( \frac{\lambda - \lambda_{\max}}{\lambda_{\max} - \lambda_{\min}} \right); \quad \text{and} \quad \lambda_N = \frac{\lambda}{\lambda_{\text{ref}}}; \quad \text{here} \quad \lambda = (U, n^*, E_x, P, Y) \quad (12)$$

where the subscripts ‘max’, ‘min’ and ‘ref’ indicate for the maximum, minimum and reference (i.e.,  $d_c = 1$ ) values of the quantity ( $\lambda$ ) for similar flow conditions ( $K, S, d_c$ ).

### 3. NUMERICAL APPROACH

In this study, the coupled mathematical model equations (Eqs. 3 to 11) have been solved using the finite element method (FEM) based COMSOL multiphysics software to obtain the electroviscous flow (EVF) fields in the charged contraction-expansion slit microfluidic device. While the detailed numerical approach is presented in recent studies [20, 27], only the salient features are included here to avoid duplication. The *Electrostatics* (es), *transport of dilute species* (tds), and *laminar flow* (spf) modules of COMSOL are used to implement the multiphysics governed by the Poisson’s (Eq. 3), Nernst-Planck (Eq. 4), and Navier-Stokes (Eqs. 5 - 6) equations, respectively. The relevant boundary conditions (Eqs. 8 to 11) are also implemented

through these multiphysics modules (es, tds, spf). Further, the integral quantities in the current continuity condition (Eq. 9) are obtained by using *intop* function in the model coupling through the ‘global function definition’. The mathematical model equations (Eqs. 3 to 11) and geometrical problem domain are discretized using the finite element method (FEM). The resulting set of coupled algebraic equations is solved iteratively using the PARDISO (PARallel DIrect SOLver), Newton’s non-linear solvers, and fully coupled method to obtain the steady-state solution for the total electrical potential ( $U$ ), induced electric field strength ( $E_x$ ), ionic concentration ( $n_{\pm}$ ), velocity ( $\mathbf{V}$ ), and pressure ( $P$ ) fields. The dimensionless geometrical characteristics (Fig. 1) are systematically optimized and obtained [18, 20, 22] as follows:  $L_u = L_c = L_d = 5$ ,  $L = 15$ , and  $0.25 \leq W_c \leq 1$ . Further, the sufficiently refined mesh, free from end effects, providing most accurate results is obtained [20] as follows:  $\Delta = 100$ , correspondingly produces ( $N_e$ , DoF) as (333600, 3018814), (358400, 3238126), (383200, 3462776) and (408000, 3687434) for  $d_c$  of 0.25, 0.50, 0.75, and 1, respectively, where  $\Delta$  is number of mesh points uniformly distributed per unit length of the boundaries,  $N_e$  is the total number of mesh elements in the computational domain (Fig. 1), and DoF is the degrees of freedom.

## 4. RESULTS AND DISCUSSION

In this section, the detailed electroviscous flow characteristics have been obtained and presented for the pressure-drive flow of electrolyte liquid in the symmetrically charged non-uniform microfluidic device by systematic variation of the following flow conditions such as surface charge density ( $4 \leq S \leq 16$ ), inverse Debye length ( $2 \leq K \leq 20$ ), and contraction

ratio ( $0.25 \leq d_c \leq 1$ ) for fixed values of Schmidt and Reynolds numbers ( $Sc = 10^3$ ;  $Re = 10^{-2}$ ). In general, the functional dependence of flow conditions ( $K, S, d_c$ ) on the total electrical potential ( $U$ ), excess ionic charge ( $n^*$ ), axially induced electric field strength ( $E_x$ ), pressure ( $P$ ) fields, and electroviscous correction factor ( $Y$ ) are presented and discussed. The considered range of conditions ( $K, S$ ) are justified [18, 20, 22, 23, 27] for their practical applicability, and discussion is not repeated here. The numerical approach used in this work has been validated [20] with the limiting literature [18] for the fixed contraction ratio ( $d_c = 0.25$ ) over the ranges of other conditions ( $K, S$ ). Based on our experience [20, 22, 23, 27], the results presented hereafter are reliable and accurate within  $\pm 1 - 2\%$ .

#### 4.1. Total electrical potential ( $U$ ) distribution

The distribution of total electrical potential ( $U$ ) along the centreline ( $0 \leq x \leq L, 0$ ) of the uniformly charged microfluidic device as a function of governing parameter ( $K, S, d_c$ ) is qualitatively similar (Fig. A.1) to that reported in the literature [18, 20, 22, 27] for no-slip flow through fixed contraction-expansion ( $d_c = 0.25$ ) microfluidic device. For instance, the potential decreases along the length of the device (i.e.,  $U \propto x^{-1}$ ), inversely proportional to the Debye parameter ( $U \propto K^{-1}$ ), and proportional to the surface charge density ( $U \propto S$ ), irrespective of the contraction size ( $d_c$ ). Further, the potential drop is highest in the contraction region compared to other regions.

Fig. 3 depicts centreline profiles of normalized total electrical potential ( $U_n$ ) in the charged microchannel for  $2 \leq K \leq 20$ ,  $4 \leq S \leq 16$ , and  $0.25 \leq d_c \leq 1$ . Centreline profiles of  $U_n$

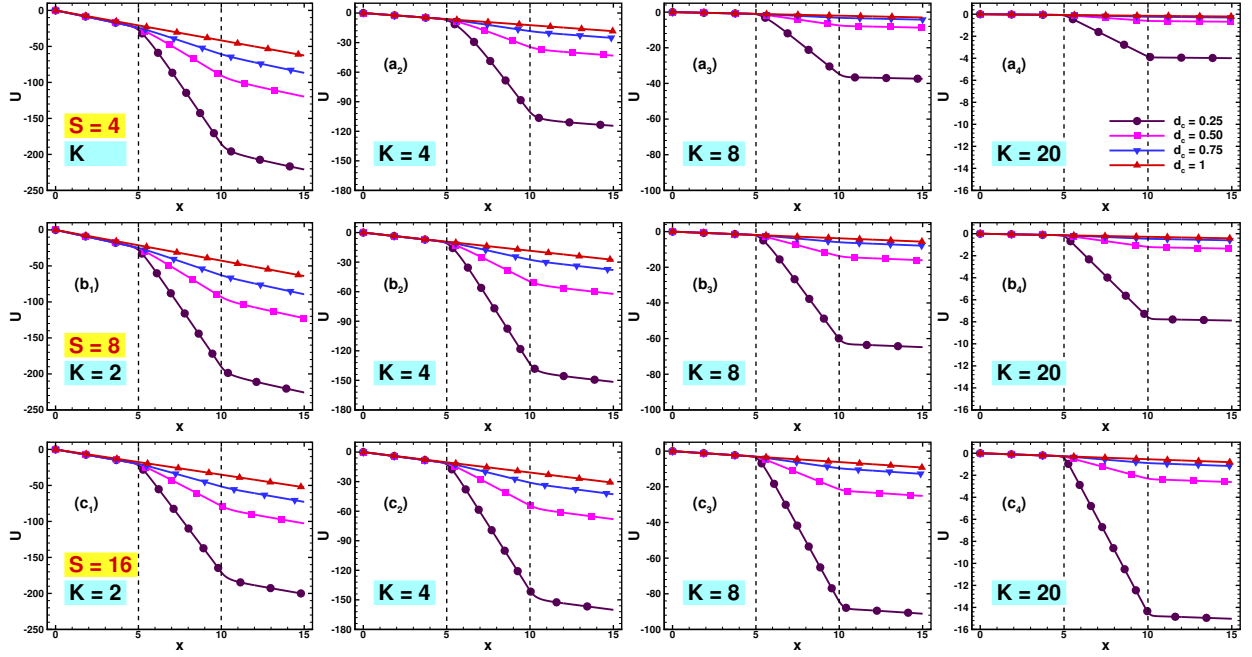


Figure 2: Total electrical potential ( $U$ ) on the centreline ( $0 \leq x \leq L, 0$ ) of charged microfluidic device as a function of dimensionless governing parameters ( $K, S, d_c$ ).

have shown similar qualitative behavior as  $U$  with the literature [18, 20, 27]. Along the length of positively charged device,  $U_n$  decreases due to advection of excess charge (negative ions) occurs as expected in the PDF direction. Normalized potential gradient is maximum in the contraction as compared to other sections (Fig. 3). Normalized potential decreases with decreasing  $K$  or EDL thickening (Fig. 3). The variation of  $U_n$  with  $K$  is maximum at higher  $d_c$  and lower  $S$ . For instance,  $|U_n|$  reduces maximally by 95.14% (0.2721 to 0.0132) when  $K$  varies from 2 to 20 at  $S = 4$  and  $d_c = 1$  (refer Fig. 3a). Normalized potential decreases with increasing  $S$  (Fig. 3a and b) but at higher  $S$ , enhances with increasing  $S$  (Fig. 3c). For instance,  $|U_n|$  increases maximally by 285.24% (0.0132 to 0.0510) when  $S$  varies from 4 to 16 at  $K = 20$  and  $d_c = 1$  (refer Fig. 3). Further,  $|U_n|$  increases with decreasing  $d_c$  (Fig. 3). The relative impact of  $d_c$  on  $U_n$  is maximum at higher  $K$  and lower  $S$  because EDLs do not occupy a greater fraction of the microfluidic device. For

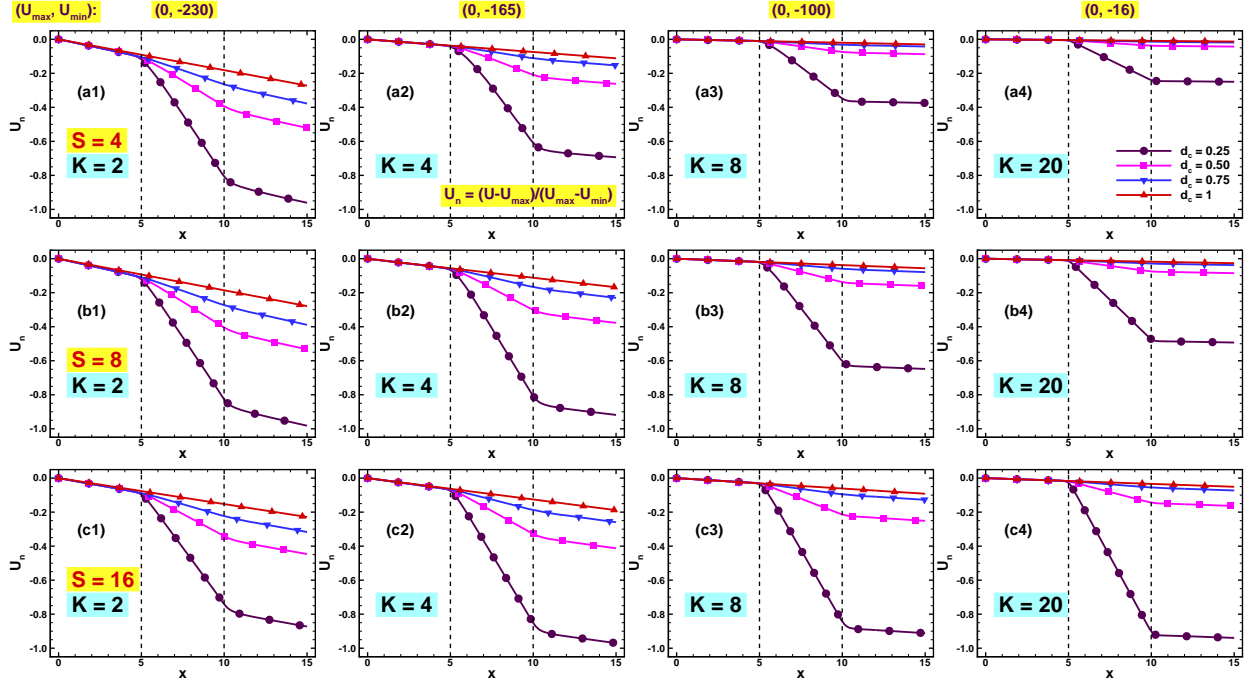


Figure 3: Centreline profiles of normalized total electrical potential ( $U_n$ ) for  $2 \leq K \leq 20$ ,  $4 \leq S \leq 16$ , and  $0.25 \leq d_c \leq 1$ .

instance,  $|U_n|$  enhances maximally by 1785.58% (0.0132 to 0.2496) when  $d_c$  varies from 1 (uniform device) to 0.25 (contraction-expansion device) at weak-EVF condition ( $K = 20$ ,  $S = 4$ ) (refer Fig. 3a4).

Subsequently, Table 1 comprises total potential drop ( $|\Delta U|$ ) on the centreline ( $0 \leq x \leq L$ , 0) of microfluidic device for wide ranges of dimensionless parameters ( $2 \leq K \leq 20$ ,  $4 \leq S \leq 16$ ,  $0.25 \leq d_c \leq 1$ ). Maximum value of potential drop ( $|\Delta U|_{\max}$ ) is underline for  $0.25 \leq d_c \leq 1$  at each combination of  $S$  and  $K$ . The variation in the value of  $|\Delta U|$  with  $K$  and  $S$  for a fixed  $d_c = 0.25$  is similar as the literature [18, 20, 27]. Potential drop ( $|\Delta U|$ ) decreases with increasing  $K$  (or EDL thinning); the decrement of  $|\Delta U|$  with  $K$  is lesser for higher  $S$  and lower  $d_c$  (Table 1). For instance,  $|\Delta U|$  reduces by (98.19%, 99.43%, 99.65%, 99.66%) and (92.51%, 97.45%, 98.40%, 98.45%) for ( $d_c = 0.25, 0.50, 0.75, 1$ ), respectively at  $S = 4$  and 16 when  $K$  varies from 2 to 20 (refer

Table 1). The  $|\Delta U|$  increases with increasing  $S$  followed by reverse trends at higher  $S$ ; it attributes due to strong charge attractive forces near the surface retards the convective flow of ions in device at higher  $S$ . The relative impact of  $S$  on  $|\Delta U|$  is maximum at higher  $K$  and  $d_c$ ; it is because EDLs overlap at lower  $K$  and higher  $S$  (Table 1). For instance,  $|\Delta U|$  varies with increasing  $S$  from 4 to 16 by (-9.14%, -14.19%, -16.07%, -15.90%) and (276.44%, 282.83%, 284.63%, 285.24%) for ( $d_c = 0.25, 0.50, 0.75, 1$ ), respectively at  $K = 2$  and 20 (refer Table 1). Further,  $|\Delta U|$  enhances with decreasing  $d_c$  because reduction in the cross-section flow area increases excess charge clustering and velocity in the microfluidic device, thus, increment in the streaming current decreases streaming potential (Table 1). For instance,  $|\Delta U|$  enhances for ( $S = 4, 8, 16$ ) by (38.66%, 39.50%, 38.37%) and (43.20%, 43.15%, 42.98%) at  $K = 2$  and 20, respectively with decreasing contraction  $d_c$  from 1 to 0.75; corresponding increment in the values of  $|\Delta U|$  for decreasing  $d_c$  from 1 to 1.50 are recorded as (91.31%, 91.42%, 95.19%) and (223.49%, 223.06%, 221.47%) at  $K = 2$  and 20. Similarly,  $|\Delta U|$  enhances at  $K = 2$  and 20 by (253.07%, 252.36%, 281.45%) and (1785.58%, 1776.40%, 1742.51%) with overall decreasing contraction  $d_c$  from 1 to 0.25 ( $0.25 \leq d_c \leq 1$ ) (refer Table 1).

Further, the relative impact of contraction ( $d_c$ ) is described by normalizing the flow fields for non-uniform ( $d_c \neq 1$ ) geometries by that at reference case of uniform ('ref' or  $d_c = 1$ ) geometry for dimensionless parameters ( $S, K$ ) as given below.

$$\theta_N = \frac{\theta}{\theta_{\text{ref}}} = \frac{\theta(d_c)}{\theta(d_c = 1)} \Big|_{S,K} \quad \text{where} \quad \theta = (U, n^*, E_x, P, Y) \quad (13)$$

For detailed analysis of total potential variation on centreline ( $0 \leq x \leq L, 0$ ) of device, it is normalized by reference potential (at  $d_c = 1$ ). Fig. 4 shows centreline profiles of normalized total electrical potential ( $U_N$ , Eq. 13) in the charged microchannel for  $2 \leq K \leq 20, 4 \leq S \leq 16$ , and

Table 1: Total electrical potential drop ( $|\Delta U|$ ), minimum value of excess charge ( $n_{\min}^*$ ), maximum value of induced electric field strength ( $E_{x,\max}$ ), and pressure drop ( $10^{-5}|\Delta P|$ ) on the centreline of device for  $2 \leq K \leq 20$ ,  $4 \leq S \leq 16$ , and  $0.25 \leq d_c \leq 1$ .

$S$	$K$	$d_c = 0.25$	0.50	0.75	1	$d_c = 0.25$	0.50	0.75	1	
		$\Delta U$				$n_{\min}^*$				
0	$\infty$	0	0	0	0	0	0	0	0	
4	2	<u>220.9700</u>	119.7300	86.7780	62.5850	<u>-6.6597</u>	-2.7279	-1.4805	-0.8159	
	4	<u>114.4300</u>	43.1980	25.3040	18.4210	<u>-1.5275</u>	-0.4923	-0.1809	-0.0662	
	6	<u>63.6860</u>	17.8980	9.2466	6.6066	<u>-0.5902</u>	-0.1267	-0.0283	-0.0063	
	8	<u>37.4060</u>	8.7252	4.2351	2.9985	<u>-0.2669</u>	-0.0357	-0.0048	-0.0007	
	20	<u>3.9929</u>	0.6850	0.3033	0.2118	<u><math>-5.3110 \times 10^{-3}</math></u>	$-3.5410 \times 10^{-5}$	$-2.3732 \times 10^{-7}$	$-1.6119 \times 10^{-9}$	
8	2	<u>225.7700</u>	122.6500	89.3850	64.0740	<u>-11.6680</u>	-4.3860	-2.2448	-1.1391	
	4	<u>151.5500</u>	62.2770	38.0280	27.7130	<u>-2.7181</u>	-0.8280	-0.3015	-0.1072	
	6	<u>99.3690</u>	30.5710	16.2210	11.6700	<u>-1.0665</u>	-0.2271	-0.0511	-0.0113	
	8	<u>64.8040</u>	16.0670	7.9006	<u>-5.6197</u>	-0.4960	-0.0669	-0.0091	-0.0012	
	20	<u>7.8852</u>	1.3576	0.6016	0.4202	<u><math>-1.0522 \times 10^{-2}</math></u>	$-7.0216 \times 10^{-5}$	$-4.6787 \times 10^{-7}$	$-3.1843 \times 10^{-9}$	
16	2	<u>200.7800</u>	102.7400	72.8350	52.6360	<u>-18.3170</u>	-6.1084	-2.9253	-1.3549	
	4	<u>160.1100</u>	68.1120	42.8220	31.1170	<u>-4.2938</u>	-1.1887	-0.4199	-0.1400	
	6	<u>122.1500</u>	41.4390	22.9800	16.7180	<u>-1.7149</u>	-0.3485	-0.0784	-0.0170	
	8	<u>91.1770</u>	25.1300	12.7710	9.1889	<u>-0.8248</u>	-0.1109	-0.0151	-0.0020	
	20	<u>15.0310</u>	2.6225	1.1664	0.8158	<u><math>-2.0306 \times 10^{-2}</math></u>	$-1.3595 \times 10^{-4}$	$-9.0796 \times 10^{-7}$	$-6.1265 \times 10^{-9}$	
		$E_{x,\max}$				$10^{-5} \Delta P $				
0	$\infty$	0	0	0	0	1.0616	0.1624	0.0678	0.0450	
4	2	<u>33.6790</u>	13.9680	7.6907	4.1720	<u>1.1673</u>	0.1896	0.0818	0.0533	
	4	<u>22.1080</u>	6.2858	2.5460	1.2281	<u>1.1189</u>	0.1715	0.0710	0.0468	
	6	<u>12.9000</u>	2.7561	0.9681	0.4406	<u>1.0952</u>	0.1658	0.0687	0.0455	
	8	<u>7.4680</u>	1.3584	0.4502	0.2000	<u>1.0811</u>	0.1638	0.0681	0.0451	
	20	<u>0.7630</u>	0.1074	0.0332	0.0142	<u>1.0629</u>	0.1624	0.0678	0.0450	
8	2	<u>33.7070</u>	14.1030	7.8680	4.2707	<u>1.2767</u>	0.2128	0.0926	0.0594	
	4	<u>26.4830</u>	8.5533	3.7429	1.8475	<u>1.2136</u>	0.1869	0.0767	0.0501	
	6	<u>18.8840</u>	4.5930	1.6844	0.7782	<u>1.1640</u>	0.1735	0.0709	0.0467	
	8	<u>12.5870</u>	2.4787	0.8372	0.3749	<u>1.1274</u>	0.1676	0.0690	0.0456	
	20	<u>1.5062</u>	0.2128	0.0658	0.0281	<u>1.0669</u>	0.1626	0.0678	0.0450	
16	2	<u>30.5860</u>	12.0150	6.4612	3.5069	<u>1.4180</u>	0.2330	0.0996	0.0633	
	4	<u>26.6960</u>	8.9506	4.1103	2.0741	<u>1.3579</u>	0.2082	0.0845	0.0544	
	6	<u>21.8890</u>	5.9714	2.3398	1.1148	<u>1.2929</u>	0.1889	0.0755	0.0492	
	8	<u>16.9910</u>	3.7871	1.3386	0.6131	<u>1.2329</u>	0.1772	0.0715	0.0469	
	20	<u>2.8667</u>	0.4105	0.1276	0.0546	<u>1.0815</u>	0.1632	0.0679	0.0450	

$0.25 \leq d_c \leq 1$ . At  $d_c < 1$ , normalized potential ( $U_N$ ) is constant in the upstream section and increases drastically in contraction section, followed by continuously decrease in downstream region. However,  $U_N$  is unity along the length at  $d_c = 1$  due to normalized by this condition (Fig. 4). The increment in the value of  $U_N$  is noted with increasing  $K$  because maximum change in the value of  $U$  with  $d_c$  is obtained at higher  $K$ , irrespective of  $S$  (refer Table 1). The relative

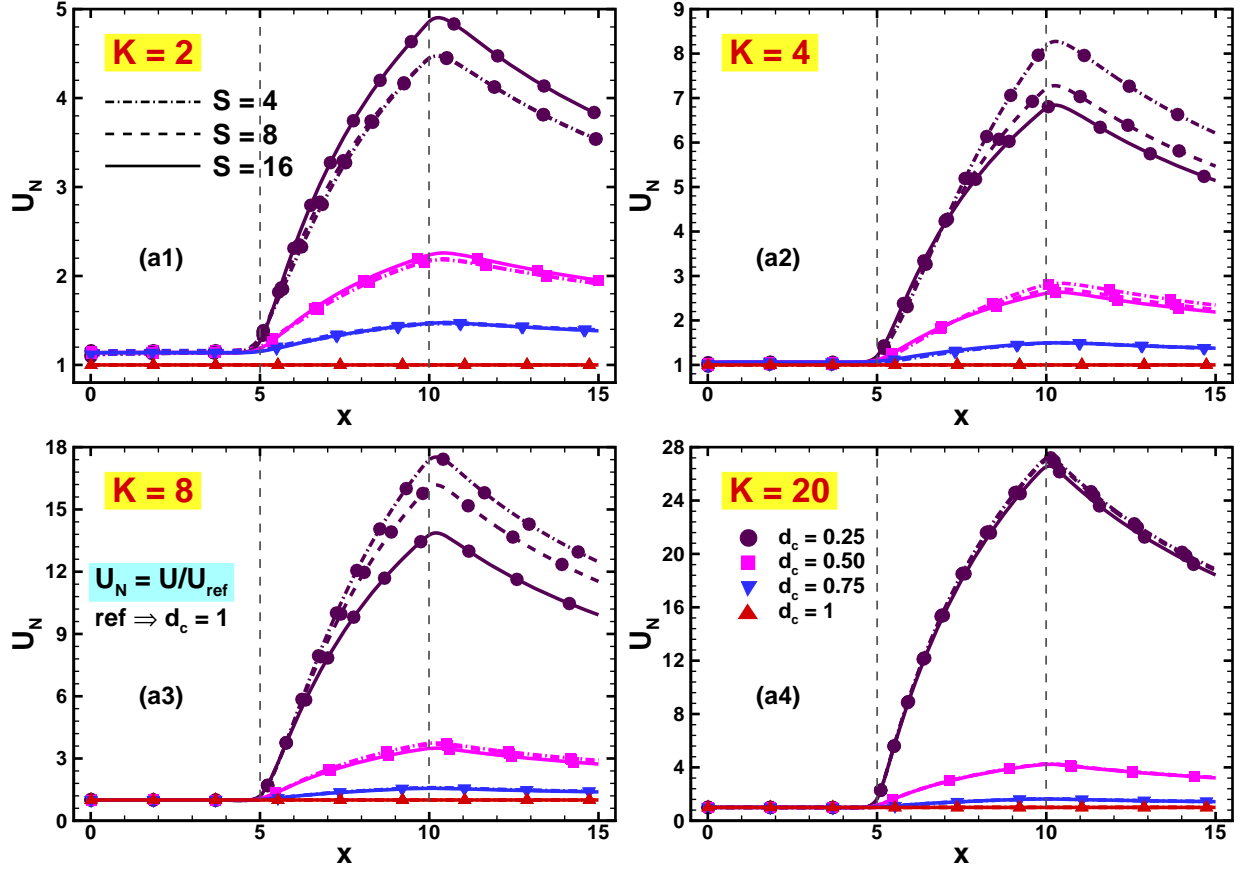


Figure 4: Centreline profiles of normalized total electrical potential ( $U_N$ ) for  $2 \leq K \leq 20$ ,  $4 \leq S \leq 16$ , and  $0.25 \leq d_c \leq 1$ .

effect of  $K$  on  $U_N$  is maximum at lower  $d_c$  and  $S$ . For instance,  $U_N$  maximally enhances by 434.05% (at  $S = 4$ ,  $d_c = 0.25$ ) when  $K$  varies from 2 to 20 (refer Fig. 4). Normalized potential increases with decreasing  $S$  (Fig. 4a2 to a4); however, it increases with increasing  $S$  at lower  $K = 2$  (thick EDL) (Fig. 4a1). It is because EDLs overlap at lower  $K$  and higher  $S$ . The variation in the value of  $U_N$  with  $S$  is maximum at  $K = 8$ . For instance,  $U_N$  reduces by 7.56% (12.4749 to 11.5316) and 20.46% (12.4749 to 9.9225) for increasing  $S$  (from 4 to 8) and (from 4 to 16), respectively at  $d_c = 0.25$  and  $K = 8$  in the end location ( $x = 10$ ) of contraction section (refer Fig. 4a3). Further,  $U_N$  enhances with decreasing  $d_c$  (Fig. 4) due to increase  $|\Delta U|$  with reducing cross-section flow



area of middle section (refer Table 1). It is because dense clustering of excess charge and velocity enhancement in that section, therefore, decrease streaming potential and increase normalized total potential. Further, the variation in the value of  $U_N$  with  $d_c$  is maximum at higher  $K$  and lower  $S$  because EDLs are thinner and do not cover greater fraction of device at this condition (Fig. 4).

Further, total potential ( $U$ ) distribution relates with excess ionic charge ( $n^*$ ) by Poisson's equation (Eq. 3). Thus, preceding section present the excess ionic charge ( $n^*$ ) as a function of governing parameters ( $S, K, d_c$ ).

## 4.2. Excess charge ( $n^*$ ) distribution

Normalized excess charge is defined as  $n_n^* = \frac{n^* - n_{\min}^*}{n_{\max}^* - n_{\min}^*}$ , here  $n_{\min}^*$  and  $n_{\max}^*$  represent the minimum and maximum values of  $n^*$  for each inverse Debye length ( $K$ ). Fig. 5 shows centreline profiles of normalized excess charge  $n_n^*$  in the charged microchannel for  $2 \leq K \leq 20$ ,  $4 \leq S \leq 16$ , and  $0.25 \leq d_c \leq 1$ . Qualitative behavior of normalized centreline excess charge profiles are same as  $n^*$  with the literature [18, 20, 27]. Normalized excess charge ( $n_n^*$ ) is equal and most prominent at horizontal centreline of channel ( $0 \leq x \leq L, 0$ ) of upstream and downstream sections in the device (Fig. 5). The  $n_n^*$  is minimum in the contraction than other sections of channel (Fig. 5). Minimum value of normalized excess charge ( $n_{n,\min}^*$ ) increases with increasing  $K$  or EDL thinning;  $n_{n,\min}^*$  values are close to zero at higher  $K = 20$  (Fig. 5). For instance,  $n_{n,\min}^*$  enhances maximally by 100% (-0.0429 to  $-3.2238 \times 10^{-8}$ ), 100% (-0.0600 to  $-6.3686 \times 10^{-8}$ ), and 100% (-0.0713 to  $-1.2253 \times 10^{-7}$ ) for  $S = 4, 8$ , and 16, respectively when  $K$

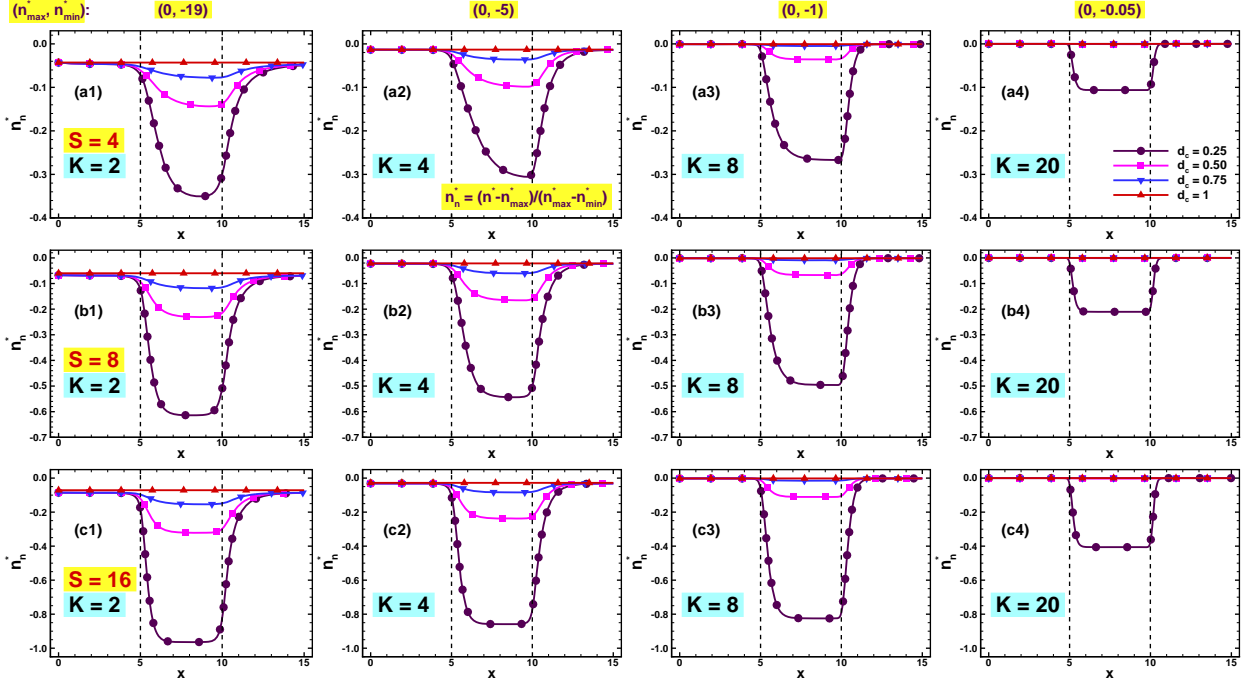


Figure 5: Centreline profiles of normalized excess charge ( $n_n^*$ ) for  $2 \leq K \leq 20$ ,  $4 \leq S \leq 16$ , and  $0.25 \leq d_c \leq 1$ .

varies from 2 to 20 at  $d_c = 1$  (refer Fig. 5). The  $n_{n,\min}^*$  decreases with increasing  $S$  (Fig. 5). For instance,  $n_{n,\min}^*$  decreases maximally by 283.93% (-0.0007 to -0.0027) when  $S$  varies from 4 to 16 at  $K = 20$  and  $d_c = 0.5$  (refer Fig. 5). Further,  $n_{n,\min}^*$  decreases with decreasing  $d_c$  (Fig. 5); the variation in the value of  $n_{n,\min}^*$  with  $d_c$  is greater at higher  $K$  and  $S$  (Fig. 5). It is because EDLs are very thin in the device at higher  $K$  and available excess ions ( $n^*$ ) in the EDL are more at higher  $S$ . For instance,  $n_{n,\min}^*$  reduces maximally by  $3.31 \times 10^8\%$  ( $-1.2253 \times 10^{-7}$  to -0.4061) when  $d_c$  varies from 1 to 0.25 at  $K = 20$  and  $S = 16$  (refer Fig. 5c4).

Subsequently, excess charge ( $n^*$ ) is minimum in the contraction than other sections of device. Table 1 summarizes the minimum excess charge ( $n_{\min}^*$ ) on the centreline ( $0 \leq x \leq L$ , 0) of microfluidic device for  $2 \leq K \leq 20$ ,  $4 \leq S \leq 16$ , and  $0.25 \leq d_c \leq 1$ . The variation of  $n_{\min}^*$  with  $K$  and  $S$  for a fixed  $d_c = 0.25$  is similar as the literature [18, 20, 27]. The  $n_{\min}^*$  increases with

increasing  $K$  (or EDL thinning); at higher inverse Debye length ( $K > 20$ ),  $n_{\min}^*$  tends to be zero (Table 1). For instance,  $n_{\min}^*$  reduces for ( $d_c = 0.25, 0.50, 0.75, 1$ ) by (99.92%, 100%, 100%, 100%) and (99.89%, 100%, 100%, 100%), respectively at  $S = 4$  and 16 when  $K$  varies from 2 to 20 (refer Table 1). The  $n_{\min}^*$  decreases with increasing  $S$  because enhancement in the electrostatic forces near the device walls, increases clustering of excess ions in the channel (Table 1). The relative effect of  $S$  on  $n_{\min}^*$  is maximum at higher  $K$ . For instance, increment in the value of  $n_{\min}^*$  are recorded with  $S$  varies from 4 to 16 as (175.04%, 123.92%, 97.59%, 66.07%) and (282.34%, 283.93%, 282.59, 280.08%) for ( $d_c = 0.25, 0.50, 0.75, 1$ ), respectively at  $K = 2$  and 20. Further,  $|n_{\min}^*|$  enhances with decreasing  $d_c$  because reduction in the cross-flow area of middle section results dense clustering of excess (negative) ions in the microfluidic device (Table 1). The variation of  $n_{\min}^*$  with  $d_c$  is maximum at higher  $K$  and  $S$ . For instance,  $n_{\min}^*$  enhances for ( $S = 4, 8, 16$ ) by (81.47%, 97.07%, 115.91%) and ( $1.46 \times 10^4\%$ ,  $1.46 \times 10^4\%$ ,  $1.47 \times 10^4\%$ ), respectively at  $K = 2$  and 20 with decreasing  $d_c$  from 1 to 0.75; corresponding increment in the values of  $n_{\min}^*$  with decreasing  $d_c$  from 1 to 0.50 are recorded as (234.36%, 285.04%, 350.84%) and ( $2.20 \times 10^6\%$ ,  $2.20 \times 10^6\%$ ,  $2.22 \times 10^6\%$ ) at  $K = 2$  and 20. Similarly,  $n_{\min}^*$  enhances at  $K = 2$  and 20 by (716.29%, 924.32%, 1251.91%) and ( $3.29 \times 10^8\%$ ,  $3.30 \times 10^8\%$ ,  $3.31 \times 10^8\%$ ) with overall decreasing contraction  $d_c$  from 1 to 0.25 ( $0.25 \leq d_c \leq 1$ ) (refer Table 1).

Further, the detailed variation of the excess charge ( $n^*$ ) on the centreline ( $0 \leq x \leq L, 0$ ) of device is explained by normalizing the excess charge with reference case (at  $d_c = 1$ ). Fig. 6 shows centreline profiles of normalized excess charge ( $n_N^*$ , Eq. 13) in the charged microchannel for  $2 \leq K \leq 20$ ,  $4 \leq S \leq 16$ , and  $0.25 \leq d_c \leq 1$ . Normalized excess charge ( $n_N^*$ ) is constant in upstream and downstream section over the horizontal centreline of device. Normalized excess

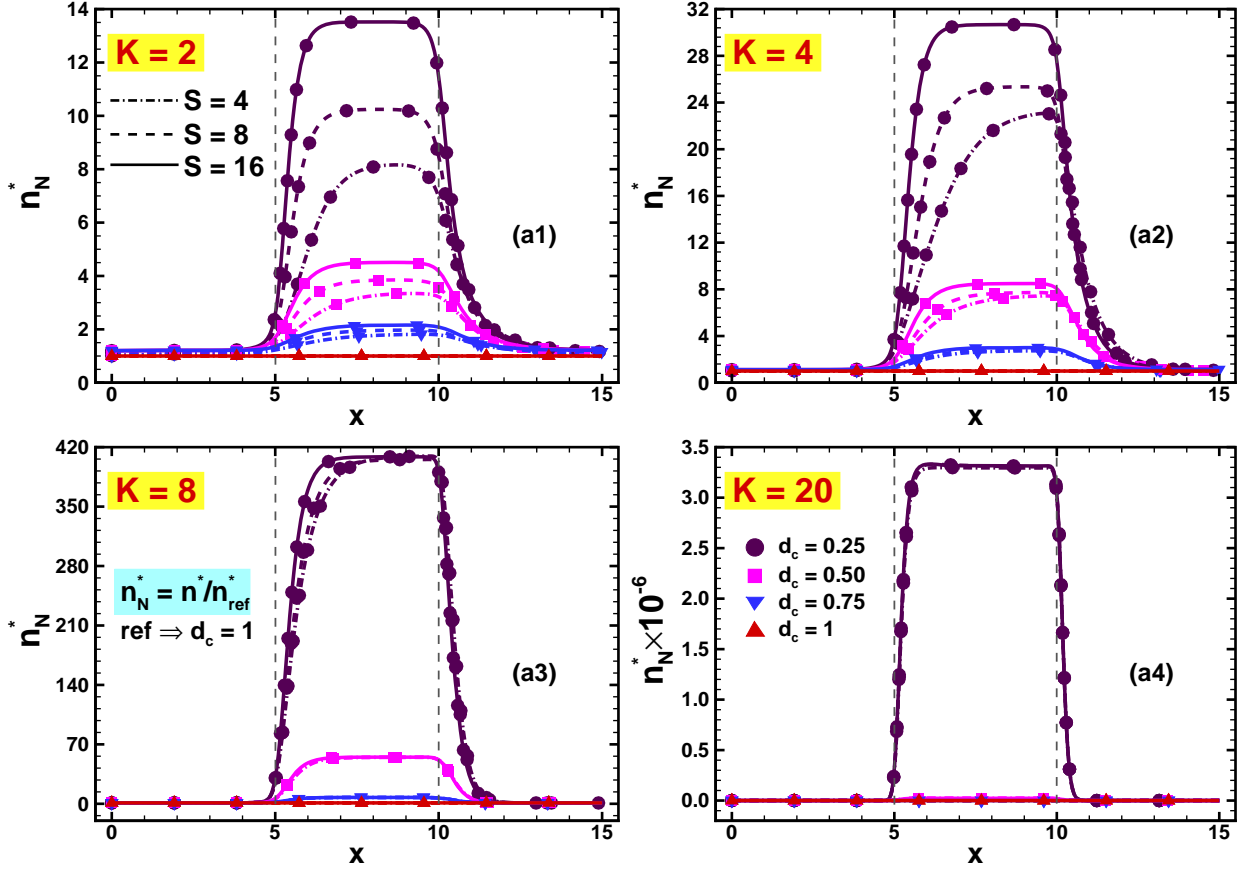


Figure 6: Centreline profiles of normalized excess charge ( $n_N^*$ ) for  $2 \leq K \leq 20$ ,  $4 \leq S \leq 16$ , and  $0.25 \leq d_c \leq 1$ .

charge ( $n_N^*$ ) is maximum in the contraction than other sections for  $d_c \neq 1$  and equal to unity for  $d_c = 1$  in the device, respectively (Fig. 6). Maximum value of normalized excess charge ( $n_{N,\max}^*$ ) increases with increasing  $K$  (Fig. 6) due to maximum variation of  $n_{\max}$  with  $d_c$  is obtained at higher  $K$ , irrespective of  $S$  (refer Table 1). For instance,  $n_{N,\max}^*$  enhances by  $4.0364 \times 10^7\%$  ( $8.1629$  to  $3.2949 \times 10^6$ ) when  $K$  changes from 2 to 20 at  $S = 4$  and  $d_c = 0.25$  (refer Fig. 6). The  $n_{N,\max}^*$  enhances with increasing  $S$  (Fig. 6); the relative impact of  $S$  on  $n_{N,\max}^*$  is maximum at lower  $K$  and  $d_c$ . For instance,  $n_{N,\max}^*$  enhances by 65.62% ( $8.1629$  to  $13.5191$ ) when  $S$  varies from 4 to 16 at  $d_c = 0.25$  and  $K = 2$  in the middle location ( $x = 7.5$ ) of contraction section (refer Fig. 6a1). Further,  $n_{N,\max}^*$  increases with decreasing  $d_c$  (Fig. 6) due to reducing cross-section area

of contraction section results dens clustering of excess ions ( $n^*$ ) in the contraction section (refer Table 1), therefore, increases normalized excess charge. The relative impact of  $d_c$  on  $n_{N,\max}^*$  is greater at higher  $K$  and  $S$  because EDLs do not overlap at this condition (Fig. 6).

### 4.3. Induced electric field strength ( $E_x$ )

The convective flow of ions in the charged microfluidic device develops an streaming current ( $I_s$ ) and potential corresponding to this current is known as streaming potential. Induced electric field strength is defined as the rate of axial variation of streaming potential (i.e.,  $E_x = -\partial U/\partial x$ ) and it is calculated from Eq. (9). Normalized induced electric field strength is defined as  $E_{x,n} = \frac{E_x - E_{x,\min}}{E_{x,\max} - E_{x,\min}}$ , here subscripts *max* and *min* denote the maximum and minimum values at each  $K$ , respectively. Fig. 7 depicts centreline profiles of normalized induced electric field strength ( $E_{x,n}$ ) in the charged microchannel for  $2 \leq K \leq 20$ ,  $4 \leq S \leq 16$ , and  $0.25 \leq d_c \leq 1$ . Centreline profiles of  $E_{x,n}$  depict qualitatively similar trends along the length of microfluidic device as  $E_x$  with the literature [20, 27]. The  $E_{x,n}$  is maximum in the contraction as compared the other sections (Fig. 7). Maximum value of induced electric field strength ( $E_{x,n,\max}$ ) increases with decreasing  $K$  of EDL thickening; the relative changes of  $E_{x,n,\max}$  with  $K$  are maximum for lower  $S$  and higher  $d_c$ . For instance,  $E_{x,n,\max}$  reduces maximally by 96.03% (0.1192 to 0.0047) when  $K$  varies from 2 to 20 at  $S = 4$  and  $d_c = 1$  (refer Fig. 7). The  $E_{x,n,\max}$  increases with increasing  $S$  followed by reverse trends at higher  $S$  (Fig. 7). The relative impact of  $S$  is maximum on  $E_{x,n,\max}$  at higher  $d_c$  and  $K$ . For instance,  $E_{x,n,\max}$  enhances maximally by 285.36% (0.0047 to 0.0182) when  $S$  varies from 4 to 16 at  $K = 20$  and  $d_c = 1$  (refer Fig. 7). Further,

$E_{x,n,\max}$  increases with decreasing  $d_c$  (Fig. 7). The variation in the value of  $E_{x,n,\max}$  with  $d_c$  is maximum at higher  $K$  and lower  $S$  because EDLs occupy the lesser fraction of device at this condition. For instance,  $E_{x,n,\max}$  enhances maximally by 5280.51% (0.0047 to 0.2543) when  $d_c$  varies from 1 to 0.25 at  $K = 20$  and  $S = 4$  (refer Fig. 7a4).

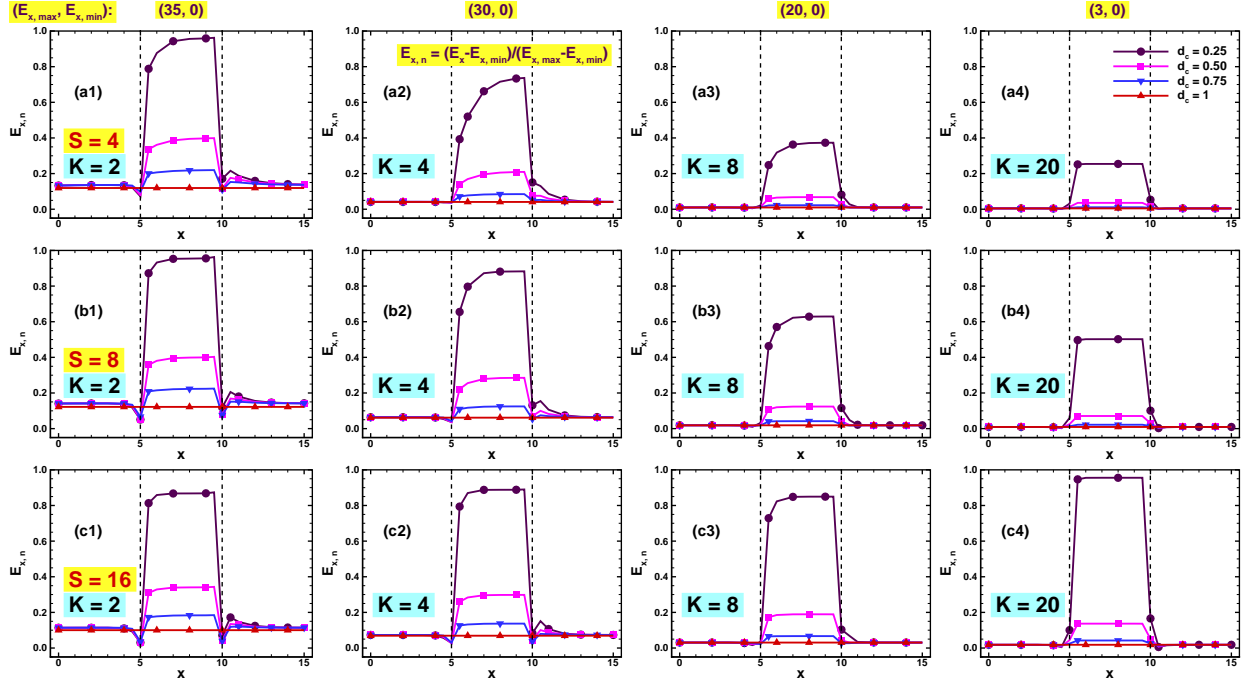


Figure 7: Centreline profiles of normalized induced electric field strength ( $E_{x,n}$ ) for  $2 \leq K \leq 20$ ,  $4 \leq S \leq 16$ , and  $0.25 \leq d_c \leq 1$ .

Further, induced electric field strength ( $E_x$ ) is maximum in the contraction than other sections of microfluidic device. Table 1 summarizes the maximum induced electric field strength ( $E_{x,\max}$ ) on centreline ( $0 \leq x \leq L$ ,  $0$ ) of microchannel for  $2 \leq K \leq 20$ ,  $4 \leq S \leq 16$ , and  $0.25 \leq d_c \leq 1$ . For a fixed  $d_c = 0.25$ , the variation of  $E_{x,\max}$  with  $S$  and  $K$  is similar as the literature [20, 27]. The  $E_{x,\max}$  increases with decreasing  $K$  or EDL thickening (Table 1); the relative effect of  $K$  on  $E_{x,\max}$  is maximum on the lower  $S$ . For instance,  $E_{x,\max}$  reduces for ( $d_c = 0.25, 0.50, 0.75, 1$ ) by (97.73%, 99.23%, 99.57%, 99.66%) and (90.63%, 96.58%, 98.03%, 98.44%), respectively at  $S = 4$  and

16 when  $K$  varies from 2 to 20 (refer Table 1). The increment in the values of  $E_{x,\max}$  are noted with increasing  $S$  but at higher  $S$ , it attributes the reverse trends due to stronger charge attractive forces near the device walls (Table 1). For instance,  $E_{x,\max}$  changes at  $K = 2$  and 20 by (-9.18%, -13.98%, -15.99%, -15.94%) and (275.71%, 282.15%, 284.52%, 285.36%) for ( $d_c = 0.25, 0.50, 0.75, 1$ ), respectively when  $S$  varies from 4 to 16 (refer Table 1). Further,  $E_{x,\max}$  enhances with decreasing  $d_c$  because reduction in the cross-flow area increases excess ions ( $n^*$ ) as discussed earlier in the section 4.2 and velocity enhancement in the channel, therefore, increases the induced electric field strength. The relative effect of  $d_c$  on  $E_{x,\max}$  is maximum at higher  $K$  and lower  $S$  (Table 1). For instance,  $E_{x,\max}$  enhances by (84.34%, 84.23%, 84.24%) and (133.99%, 133.88%, 133.48%) for ( $S = 4, 8, 16$ ), respectively at  $K = 2$  and 20 with  $d_c$  varies from 1 to 0.75; corresponding increment in the values of  $E_{x,\max}$  with decreasing  $d_c$  from 1 to 0.50 are recorded as (234.80%, 230.23%, 242.61%) and (657.41%, 656.14%, 651.12%), respectively at  $K = 2$  and 20. Similarly,  $E_{x,\max}$  increases by (707.26%, 689.26%, 772.17%) and (5280.51%, 5251.95%, 5145.75%), at  $K = 2$  and 20, respectively with overall decreasing contraction  $d_c$  from 1 to 0.25 ( $0.25 \leq d_c \leq 1$ ) (refer Table 1).

Subsequently, for detailed investigation of induced electric field strength ( $E_x$ ) variation on the centreline ( $0 \leq x \leq L, 0$ ) of device, it is normalized by reference case (at  $d_c = 1$ ). Fig. 8 represents centreline profiles of normalized induced electric field strength ( $E_{x,N}$ , Eq. 13) in the charged microchannel for  $2 \leq K \leq 20, 4 \leq S \leq 16$ , and  $0.25 \leq d_c \leq 1$ . Normalized induced electric field strength ( $E_{x,N}$ ) variation along the length is similar qualitatively as  $E_{x,n}$  (Fig. 7). The  $E_{x,N}$  is maximum in the contraction as compared to upstream and downstream sections of device (Fig. 8). Maximum normalized induced electric field strength ( $E_{x,N,\max}$ ) increases with

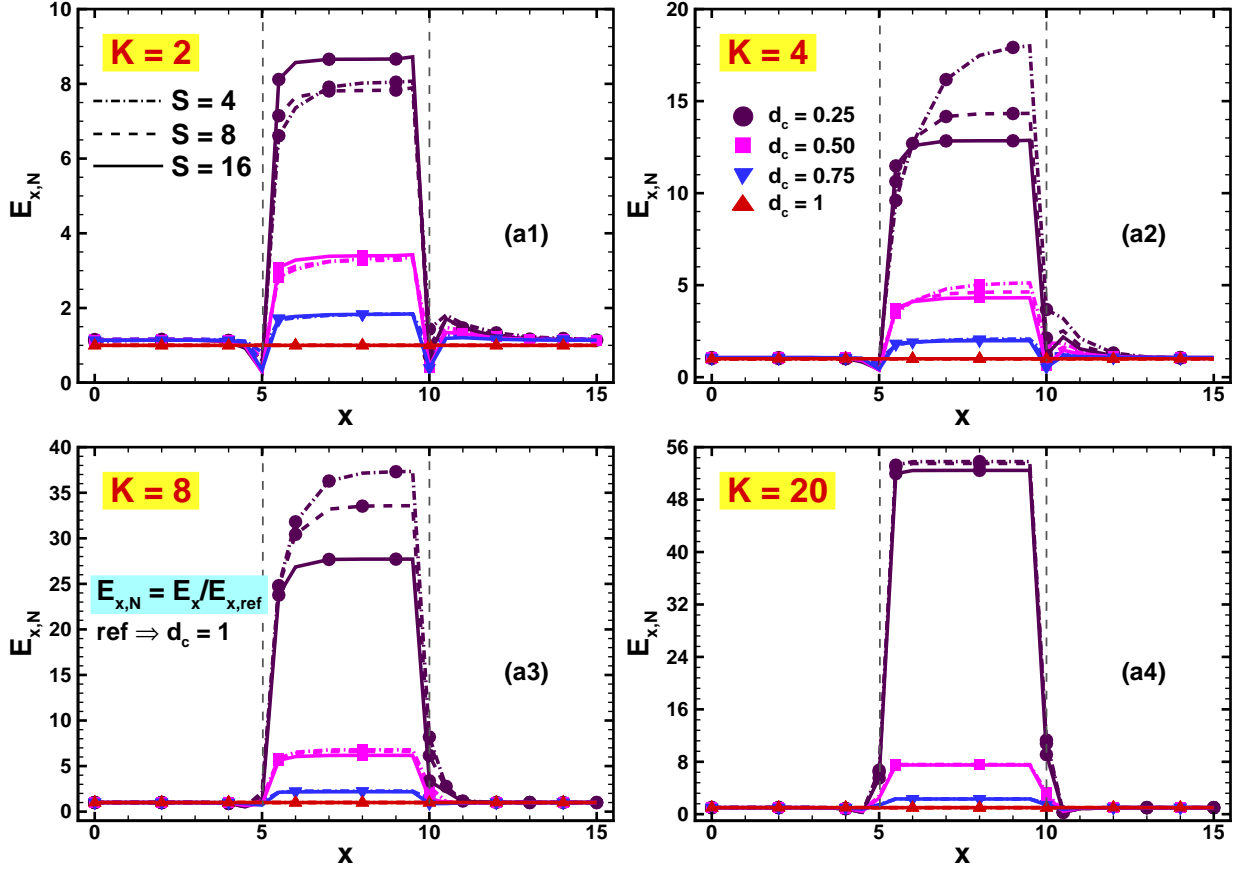


Figure 8: Centreline profiles of normalized induced electric field strength ( $E_{x,N}$ ) for  $2 \leq K \leq 20$ ,  $4 \leq S \leq 16$ , and  $0.25 \leq d_c \leq 1$ .

increasing  $K$  (Fig. 8) because  $E_{x,\max}$  variation with  $d_c$  is greater at higher  $K$ , irrespective of  $S$  (refer Table 1). For instance, maximum enhancement in  $E_{x,N,\max}$  is noted as 578.10% (7.8926 to 53.5195) at  $d_c = 0.25$  and  $S = 8$  when  $K$  changes from 2 to 20 (refer Fig. 8). The  $E_{x,N,\max}$  enhances with decreasing  $S$  but it has shown reverse trends at  $K = 2$  (Fig. 8a1); the change of  $E_{x,N,\max}$  with  $S$  is depicted maximum at  $K = 4$ . For instance,  $E_{x,N,\max}$  reduces by 20.37% (18.0018 to 14.3345) and 28.50% (18.0018 to 12.8711) with increasing  $S$  (from 4 to 8) and (from 4 to 16), respectively at  $d_c = 0.25$  and  $K = 4$  in the contraction section ( $x = 8$ ) of device (refer Fig. 8a2). Further,  $E_{x,N,\max}$  increases with decreasing  $d_c$  due to reduction in the constricted flow area of



middle section of device (Fig. 8). It is because more excess charge transport due to clustering of  $n^*$  (refer section 4.2) and velocity enhancement, increases  $E_x$  and hence normalized induced electric field strength. The relative impact of  $d_c$  on  $E_{x,N,\max}$  is noted maximum at lower  $S$  and higher  $K$  due to maximum relative variation of  $E_x$  for identical ranges of conditions (refer Table 1).

The preceding discussion has depicted stronger dependence of electrostatic and ionic fields such as total electrical potential ( $U$ ), excess ionic charge ( $n^*$ ), and induced electric field strength ( $E_x$ ) on governing parameters ( $S$ ,  $K$ ,  $d_c$ ). The next section presents an analysis of the corresponding influences on pressure ( $P$ ).

#### 4.4. Velocity ( $\mathbf{V}$ ) field

Velocity ( $\mathbf{V}$ ) field distribution in the considered microfluidic device for  $0.25 \leq d_c \leq 1$ ,  $K = 2$  and  $S = 8$  is depicted in the Fig. 9. Contours for other ranges of condition ( $2 \leq K \leq 20$ ,  $4 \leq S \leq 16$ ,  $0.25 \leq d_c \leq 1$ ) are qualitatively similar, thus not presented here. Velocity ( $\mathbf{V}$ ) field increases from surface to centreline due to no-slip condition at the walls of microfluidic device. Therefore, the maximum value of  $\mathbf{V}$  is obtained at the centreline of device. In addition,  $\mathbf{V}$  enhances with decreasing  $d_c$  due to reduction in the cross-section area at the fixed volumetric flow rate (i.e.,  $Q = A\mathbf{V} = A_c\mathbf{V}_c = \text{constant}$ ). For instance, maximum value of  $\mathbf{V}$  varies from 1.55 to 6.04 with decreasing  $d_c$  from 1 to 0.25 at  $K = 2$  and  $S = 8$  (Fig. 9). However, overall maximum value of  $\mathbf{V}$  is obtained as 6.11 at  $d_c = 0.25$ ,  $K = 2$  and  $S = 16$  (Table 2).

Fig. 10 shows the centreline ( $x, 0$ ) profiles of velocity ( $\mathbf{V}$ ) field in the considered microfluidic

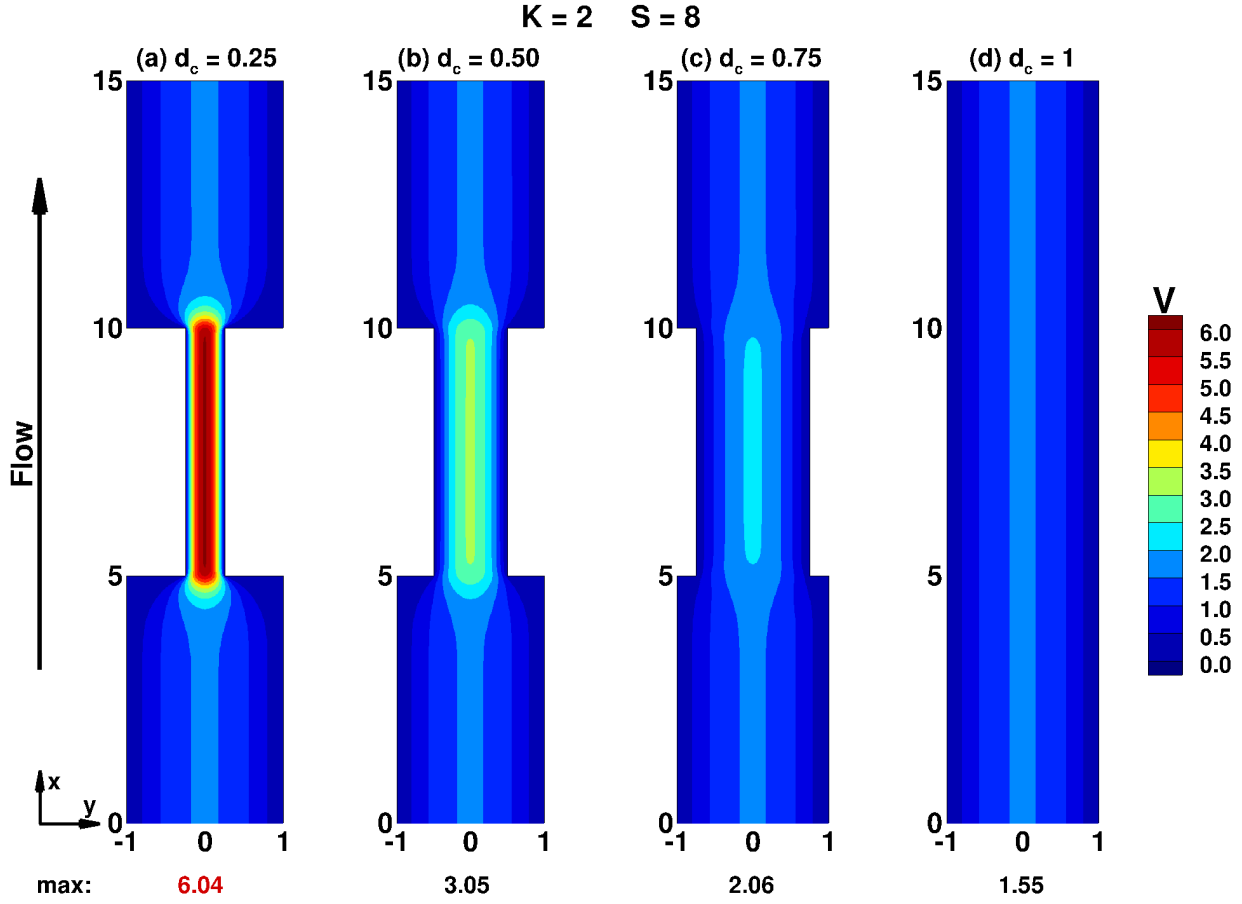


Figure 9: Velocity ( $V$ ) field distribution for  $0.25 \leq d_c \leq 1$  at  $K = 2$  and  $S = 8$ .

device for  $2 \leq K \leq 20$ ,  $4 \leq S \leq 16$ , and  $0.25 \leq d_c \leq 1$ . The  $V$  has shown the complex variation along the length of device, irrespective of  $K$  and  $S$ . For instance,  $V$  is constant in the upstream section followed by the steep enhance in the end of section. In contraction region,  $V$  is constant throughout the section. Further, in downstream section,  $V$  reduces in the starting of the section and becomes constant in the latter part of the section. Thus, the maximum velocity ( $V_{\max}$ ) is observed in the contraction than other sections of device. However,  $V$  is constant throughout the channel at  $d_c = 1$ , irrespective of  $K$  and  $S$ . The  $V_{\max}$  has depicted the strong dependence on  $d_c$  and insignificant dependence on  $K$  and  $S$ . The increment in  $V_{\max}$  is noted with decreasing

$d_c$ . It is because at constant flow rate ( $Q$ ), suddenly constricted flow area with reduction in  $d_c$  increases  $V_{\max}$ . For instance,  $V_{\max}$  for non-electroviscous ( $S = 0$  or  $K = \infty$ ) flow is obtained as (1.5, 2, 3, 6) at ( $d_c = 1, 0.75, 0.50, 0.25$ ), respectively. The  $V_{\max}$  increases from (1.52 to 6.01), (1.55 to 6.04), and (1.58 to 6.11) for ( $S = 4, 8,$  and  $16$ ), respectively with the variation of  $d_c$  from 1 to 0.25 at  $K = 2$ . Corresponding enhancement in  $V_{\max}$  is recorded as (1.50 to 6), (1.50 to 6.01), and (1.50 to 6.02) at  $K = 20$  (Table 2). Further, slight increment in  $V_{\max}$  is observed with decreasing  $K$  and increasing  $S$  due to enhances electrostatic forces near the device walls.

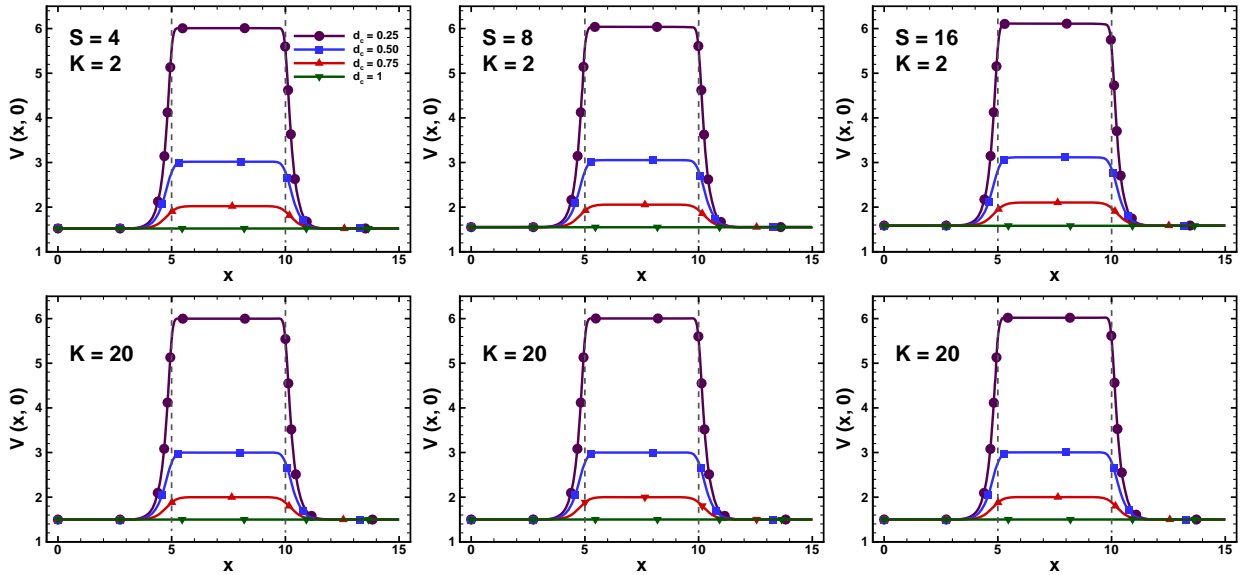


Figure 10: Centreline profiles of velocity ( $V$ ) field for  $2 \leq K \leq 20$ ,  $4 \leq S \leq 16$ , and  $0.25 \leq d_c \leq 1$ .

Subsequently, Fig. 11 represents the velocity ( $V$ ) field variation over the vertical length ( $L/2, y$ ) in the middle section of considered microfluidic device for  $2 \leq K \leq 20$ ,  $4 \leq S \leq 16$  and  $0.25 \leq d_c \leq 1$ . The increment in  $V$  is noted (0 to  $V_{\max}$ ) from walls to centreline of device. It is because no-slip condition is used at the devices walls. The  $d_c$  has significantly affected  $V_{\max}$ , irrespective of  $K$  and  $S$ . The enhancement in  $V_{\max}$  is obtained with reducing  $d_c$ . However,

Table 2: Maximum velocity ( $V_{\max}$ ) on the centreline of charged microfluidic device as function of governing parameters ( $K$ ,  $S$ , and  $d_c$ ).

$S$	$K$	$V_{\max}$			
		$d_c = 0.25$	$d_c = 0.50$	$d_c = 0.75$	$d_c = 1$
0	$\infty$	6	3	2	1.5
4	2	6.0102	3.0183	2.0220	1.5209
	20	6.0015	2.9997	1.9992	1.4991
8	2	6.0399	3.0537	2.0561	1.5491
	20	6.0061	3.0007	1.9996	1.4993
16	2	6.1129	3.1173	2.1034	1.5818
	20	6.0229	3.0047	2.0010	1.4999

relatively less increment is noted in  $V_{\max}$  with enhancing  $S$  and decreasing  $K$ . It is because strong electrostatic forces reduce  $V_{\max}$  in the close vicinity of walls, thus, increases  $V_{\max}$  on the centreline of device.

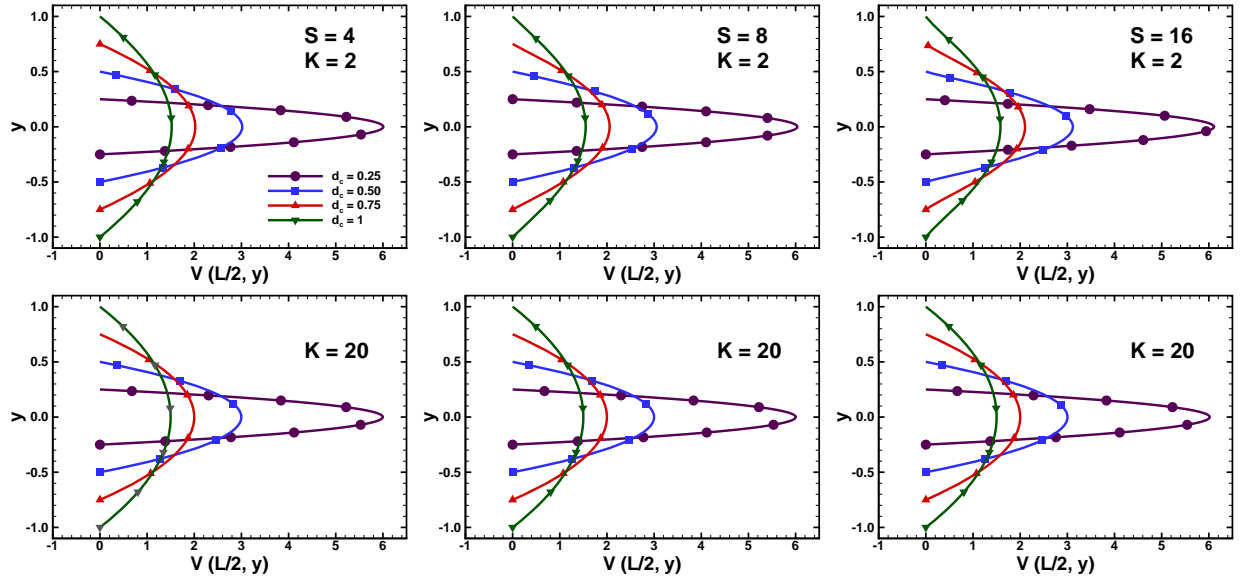


Figure 11: Velocity ( $V$ ) field variation over the vertical length ( $L/2$ ,  $y$ ) in the contraction for  $2 \leq K \leq 20$ ,  $4 \leq S \leq 16$ , and  $0.25 \leq d_c \leq 1$ .

## 4.5. Pressure ( $P$ ) distribution

Normalized pressure is defined as  $P_n = \frac{P - P_{\min}}{P_{\max} - P_{\min}}$ , here subscripts *min* and *max* denote minimum and maximum value of  $P$  for each  $K$ . Fig. 12 depicts centreline profiles of normalized pressure ( $P_n$ ) in the charged microchannel for  $2 \leq K \leq 20$ ,  $4 \leq S \leq 16$ , and  $0.25 \leq d_c \leq 1$ . The  $P_n$  decreases along the length of microfluidic device (Fig. 12) due to imposed additional hydrodynamic resistance on the fluid by increased  $|\Delta U|$  along the length as we have discussed in the section 4.1. Normalized pressure gradient is maximum in the contraction section because of applied additional resistance by both charge attractive and hydrodynamic forces with sudden constricted flow area (Fig. 12). Qualitative behavior of centreline  $P_n$  profiles are same as  $P$  with the literature [18, 20]. Normalized pressure has shown complex dependency on  $K$ ,  $S$ , and  $d_c$ . For instance,  $|P_n|$  enhances maximally by 24.17% (0.7782 to 0.9663) when  $K$  varies from 2 to 20 at  $S = 4$  and  $d_c = 0.25$  (refer Fig. 12a). The  $P_n$  decreases with increasing  $S$  (Fig. 12). For instance,  $|P_n|$  increases maximally by 22.89% (0.1264 to 0.1553) when  $S$  varies from 4 to 16 at  $K = 2$  and  $d_c = 0.50$  (refer Fig. 12). Further,  $|P_n|$  enhances with decreasing  $d_c$  (Fig. 12). The variation in the value of  $P_n$  with  $d_c$  is greater at higher  $K$  and  $S$ . For instance, maximum increment in the value of  $|P_n|$  is noted as 2526.38% (0.0361 to 0.9484) when  $d_c$  varies from 1 to 0.25 at  $K = 8$  and  $S = 16$  (refer Fig. 12c3).

Subsequently, Table 1 comprises the pressure drop ( $|\Delta P|$ ) on centreline ( $0 \leq x \leq L$ , 0) of device for  $2 \leq K \leq 20$ ,  $4 \leq S \leq 16$ , and  $0.25 \leq d_c \leq 1$ . The  $\Delta P$  variation with  $K$  and  $S$  is similar as the literature [18, 20, 27] for a fixed  $d_c = 0.25$ . Pressure drop ( $|\Delta P|$ ) increases with decreasing  $K$  or EDL thickening; the change in the values of  $|\Delta P|$  with  $K$  are maximum at

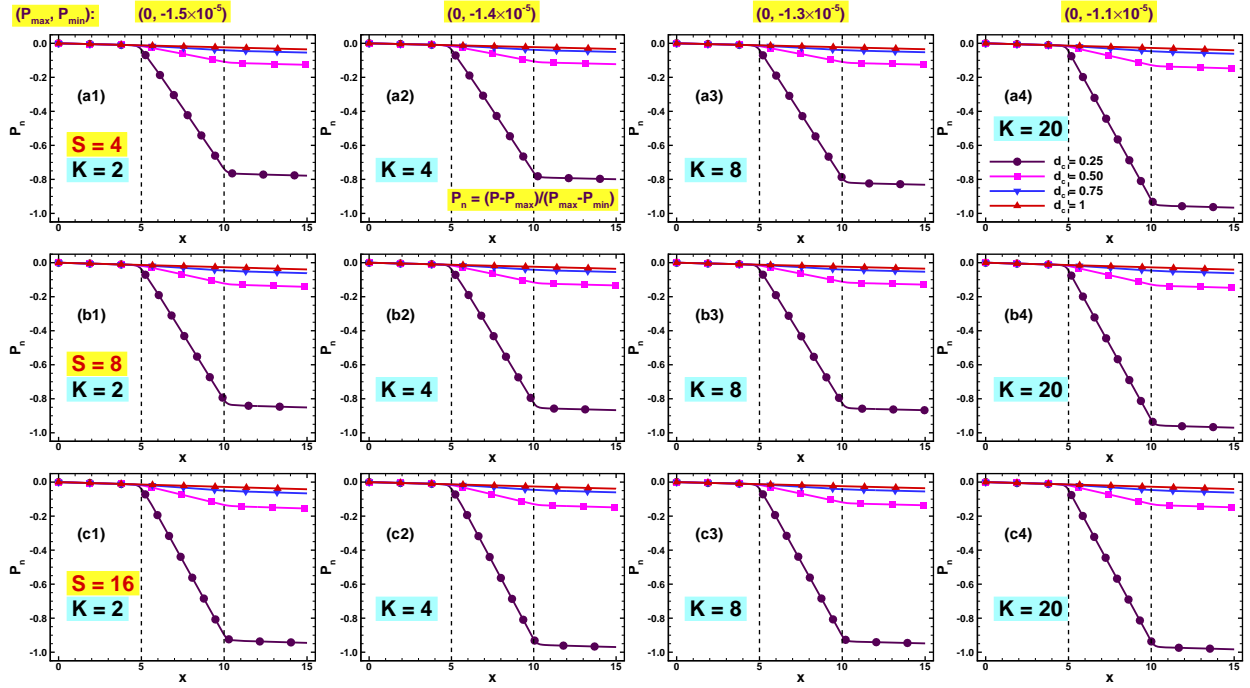


Figure 12: Centreline profiles of normalized pressure ( $P_n$ ) for  $2 \leq K \leq 20$ ,  $4 \leq S \leq 16$ , and  $0.25 \leq d_c \leq 1$ .

higher  $S$  (Table 1). For instance, pressure drop ( $|\Delta P|$ ) reduces by (8.94%, 14.35%, 17.12%, 15.57%) and (23.73%, 29.95%, 31.80%, 28.78%) for ( $d_c = 0.25, 0.50, 0.75, 1$ ) at  $S = 4$  and 16 when  $K$  varies from 2 to 20 (refer Table 1). The  $|\Delta P|$  enhances with increasing  $S$  due to additional resistance imposed by charge attractive forces with increasing  $S$  (Table 1). The relative effect of  $S$  on  $|\Delta P|$  is maximum at thick EDL (lower  $K$ ). For instance, increment in  $|\Delta P|$  is recorded at  $K = 2$  and 20 as (21.48%, 22.89%, 21.82%, 18.77%) and (1.75%, 0.51%, 0.24%, 0.18%) for ( $d_c = 0.25, 0.50, 0.75, 1$ ), respectively when  $S$  varies from 4 to 16 (refer Table 1). Further,  $|\Delta P|$  increases with decreasing  $d_c$  (Table 1) because enhancement in the additional hydrodynamic resistance on the fluid applied by increase total potential with reducing  $d_c$  as discuss in the section 4.1. The variation in the value of  $|\Delta P|$  with  $d_c$  is maximum at higher  $S$  and  $K$ . For instance,  $\Delta P$  enhances for ( $S = 4, 8, 16$ ) by (53.54%, 56.06%, 57.48%) and (50.72%, 50.74%, 50.82%), respectively

at  $K = 2$  and  $20$  when  $d_c$  varies from  $1$  to  $0.75$ ; corresponding increment in the values of  $|\Delta P|$  are recorded as  $(256.02\%, 258.54\%, 268.39\%)$  and  $(261.17\%, 261.42\%, 262.38\%)$  with decreasing  $d_c$  from  $1$  to  $0.50$ . Similarly,  $\Delta P$  increases by  $(2091.78\%, 2050.67\%, 2141.79\%)$  and  $(2263.68\%, 2271.73\%, 2300.83\%)$ , respectively at  $K = 2$  and  $20$  with overall decreasing contraction  $d_c$  from  $1$  to  $0.25$  ( $0.25 \leq d_c \leq 1$ ) (refer Table 1).

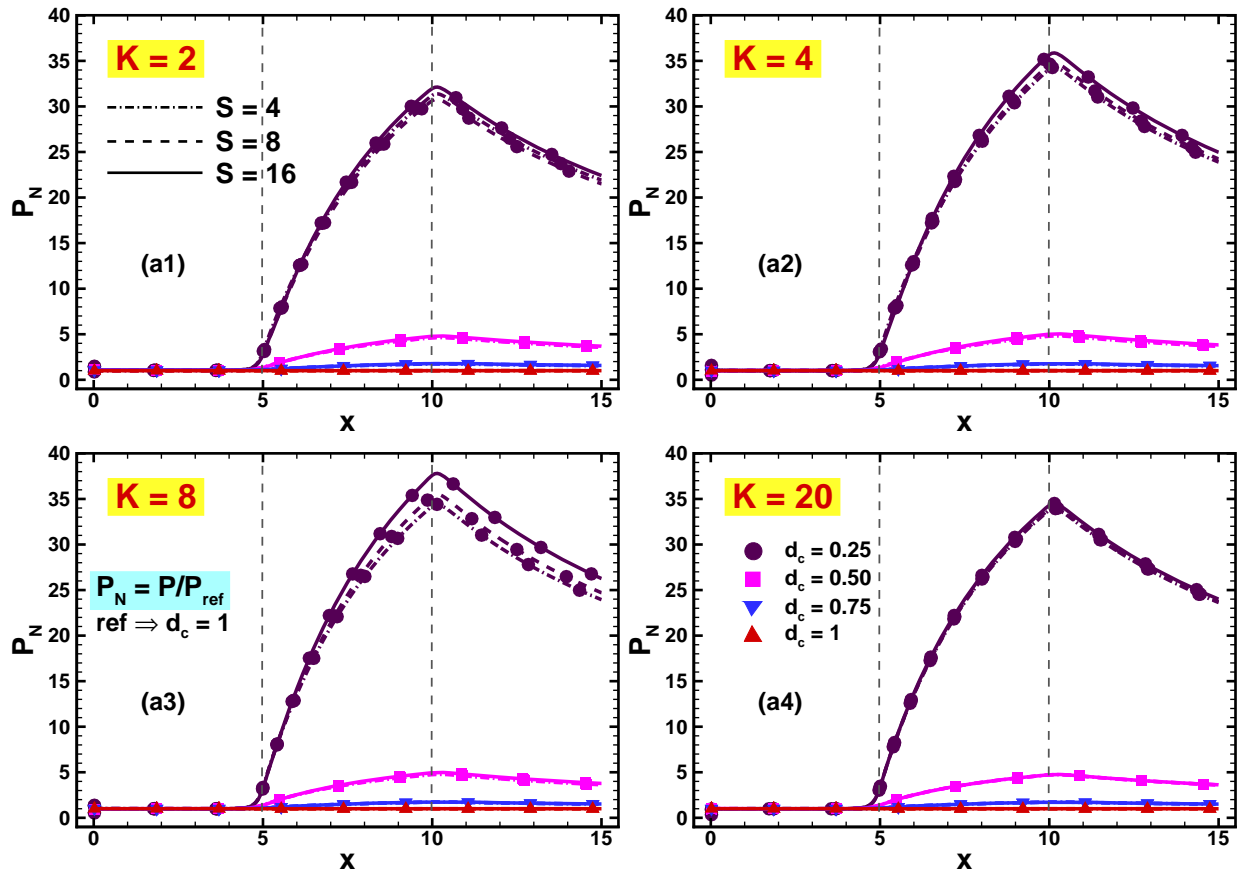


Figure 13: Centreline profiles of normalized pressure ( $P_N$ ) for  $2 \leq K \leq 20$ ,  $4 \leq S \leq 16$ , and  $0.25 \leq d_c \leq 1$ .

Further, pressure ( $P$ ) is normalized by reference case (at  $d_c = 1$ ) for detailed investigation of pressure variation along the centreline ( $0 \leq x \leq L$ ,  $0$ ) of microfluidic device. Fig. 13 depicts centreline profiles of normalized pressure ( $P_N$ , Eq. 13) in the charged microchannel for  $2 \leq K \leq 20$ ,  $4 \leq S \leq 16$ , and  $0.25 \leq d_c \leq 1$ . Normalized pressure ( $P_N$ ) qualitative variation

along the length of microfluidic device is same as  $U_N$  discussed in the section 4.1 (refer Fig. 4). Normalized pressure increases with increasing  $K$  (Fig. 13) because the variation of  $P$  with  $d_c$  is greater at higher  $K$ , irrespective of  $S$  (Table 1). For instance, maximum increment in the value of  $P_N$  is noted as 10.28% (21.5067 to 23.7173) when  $K$  changes from 2 to 20 at  $d_c = 0.25$  and  $S = 8$  (refer Fig. 13). Normalized pressure increases with decreasing  $S$ ; variation in the value of  $P_N$  with  $S$  is maximum at  $K = 8$  (Fig. 13). For instance,  $P_N$  enhances by 3.18% (23.9478 to 24.7101) and 9.67% (23.9478 to 26.2638) with increasing  $S$  (from 4 to 8) and (from 4 to 16), respectively at  $d_c = 0.25$  and  $K = 8$  in the end location ( $x = 10$ ) of contraction section (refer Fig. 13a3). Further,  $P_N$  increases with decreasing  $d_c$  due to reducing area of cross-section in the contraction section. It is because enhances convective transport of excess ions in the device, decreases total potential (refer section 4.1). Therefore, it is imposed a additional hydrodynamic force on the fluid and increases normalized pressure (Fig. 13). The relative impact of  $d_c$  on  $P_N$  is maximum at higher  $K$  and lower  $S$  because EDLs do not occupy the greater fraction of microfluidic device (Fig. 13).

#### 4.6. Electroviscous correction factor ( $Y$ )

In the electrokinetic flows, the convective transport of excess ions ( $n^*$ ) develops a induced electric field strength ( $E_x$ ) that imposes a additional hydrodynamic resistance on the fluid flow in the microfluidic device. This extra hydrodynamic resistance manifests a pressure drop ( $\Delta P$ ) that is greater than the pressure drop ( $\Delta P_0$ ) excluding electrical body forces ( $S = 0$ ) at the fixed volumetric flow rate ( $Q$ ). It is generally described as the apparent viscosity ( $\mu_{\text{eff}}$ ) that is the



viscosity needed to acquire pressure drop ( $\Delta P$ ) in the absence of electrical body forces ( $S = 0$ ). Further, it is quantified as the ‘electroviscous effect’ (EVE) [18, 20, 22]. For low Reynolds number steady laminar Poiseuille flow, the non-linear advection term in the momentum equation (Eq. 6) becomes negligible. The relative enhancement in the pressure drop ( $\Delta P/\Delta P_0$ ) relates the relative enhancement in the viscosity ( $\mu_{\text{eff}}/\mu$ ) of fluid, under otherwise identical conditions. Thus, *electroviscous correction factor* ( $Y$ ) is expressed as follows.

$$Y = \frac{\mu_{\text{eff}}}{\mu} = \frac{\Delta P}{\Delta P_0} \quad (14)$$

where  $\mu$  is viscosity of liquid yielding the pressure drop ( $\Delta P_0$ ).

Fig. 14a represents electroviscous correction factor ( $Y$ ) as a function of  $2 \leq K \leq 20$ ,  $4 \leq S \leq 16$ , and  $0.25 \leq d_c \leq 1$ . Electroviscous effects are stronger when  $Y > 1$  and absent when  $Y = 1$ . The factor ( $Y$ ) shows significant dependency on  $K$  and  $S$ , irrespective of  $d_c$ . The  $Y$  depicts similar behavior with  $K$  and  $S$  as the literature [18, 20] for a fixed  $d_c = 0.25$ . The correction factor ( $Y$ ) decreases with increasing  $K$  (EDL thinning) and increases with increasing  $S$  for a fixed  $d_c$  (Fig. 14a). For instance,  $Y$  enhances by 31.80% (at  $S = 16$ ,  $d_c = 0.75$ ) and 22.89% (at  $K = 2$ ,  $d_c = 0.50$ ) with decrement of  $K$  (from 20 to 2) and increment of  $S$  (from 4 to 16), respectively (refer Fig. 14a).

The factor ( $Y$ ) has shown complex dependency on  $d_c$ . At  $K > 4$ ,  $Y$  increases with decreasing  $d_c$  for  $4 \leq S \leq 16$  (Fig. 14a). It is because reduction in the contraction area enhances velocity and hence pressure drop (i.e.,  $\Delta P \propto \mathbf{V}$  for a channel flow by *Hagen-Poiseuille* relation), therefore,  $Y$  increases from Eq. (14). However, at  $K = 4$ , the variation of  $Y$  with  $d_c$  has shown the cross-over point (Fig. 14a). At  $K < 4$ ,  $Y$  is obtained maximum (at  $d_c = 0.75$ ) and minimum (at  $d_c = 0.25$ )

for  $4 \leq S \leq 16$  (Fig. 14a). Further, at  $K = 2$ ,  $Y$  increases with  $d_c$  varies from 0.25 followed by 0.50, 1, and 0.75, respectively for  $S = 4, 8$ ; corresponding  $Y$  enhances with  $d_c$  changes from 0.25 followed by 1, 0.50, and 0.75, respectively for  $S = 16$ . It is because EDLs start to overlap at lower  $K \leq 4$ , therefore, such complex behavior is obtained over given ranges of conditions. Overall increment in  $Y$  is noted as 46.99% (at  $K = 2, S = 16, d_c = 0.75$ ), relative to non-EVF ( $S = 0$ ) (refer Fig. 14a).

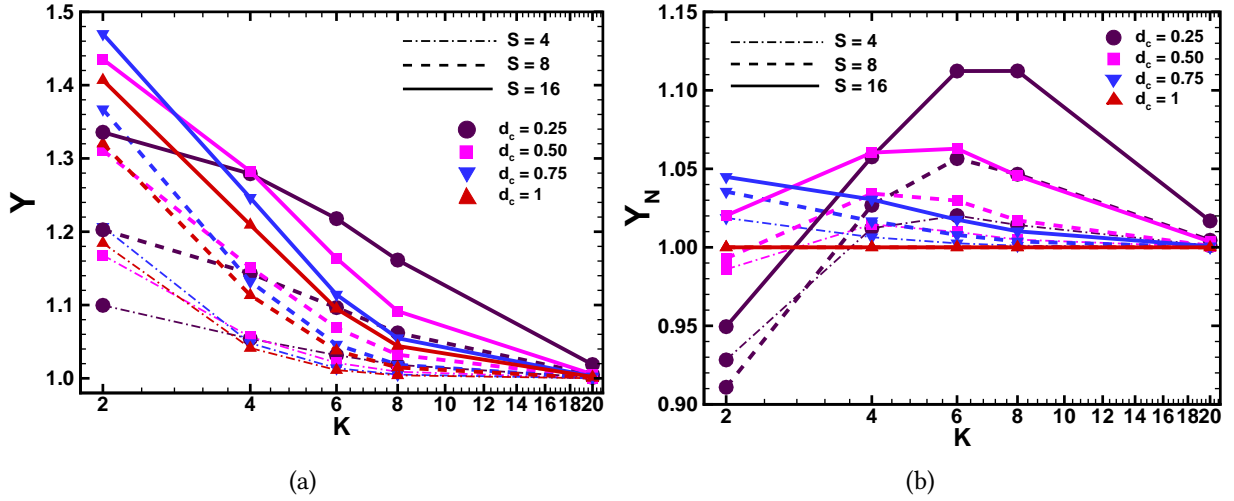


Figure 14: (a) Electroviscous correction factor ( $Y$ ), (b) Normalized electroviscous correction factor ( $Y_N$ ).

Further, the complex variation of factor ( $Y$ ) with governing parameters ( $K, S, d_c$ ) is understood in detailed by normalizing  $Y$  with uniform ( $d_c = 1$ ) geometry case. Fig. 14b depicts the normalized electroviscous correction factor ( $Y_N$ , Eq. 13) as a function of dimensionless parameters ( $2 \leq K \leq 20, 4 \leq S \leq 16, 0.25 \leq d_c \leq 1$ ). The  $Y_N$  is equal to unity for  $d_c = 1$  due to normalizing with that case (Fig. 14b). Normalized factor ( $Y_N$ ) shows complex dependency on  $K, S$ , and  $d_c$ . The  $Y_N$  increases with increasing  $S$ , irrespective of the  $K$  and  $d_c$  (Fig. 14b). The  $Y_N$  decreases with increasing  $K$  for  $d_c = 0.75$  and  $4 \leq S \leq 16$ ;  $Y_N$  increases for  $2 \leq K \leq 4$  and decreases for

$4 \leq K \leq 20$ , respectively at  $d_c = 0.50$  and  $4 \leq S \leq 16$ . However,  $Y_N$  increases for  $2 \leq K \leq 6$  and reduces for  $6 \leq K \leq 20$  at  $d_c = 0.25$  and  $4 \leq S \leq 16$  (Fig. 14b). For instance,  $Y_N$  maximally increases by 10.28% ( $S = 8, d_c = 0.25$ ) when  $K$  varies from 2 to 20. Normalized correction factor has also shown complex variation with  $d_c$  similar as  $Y$  for given ranges of  $2 \leq K \leq 20$  and  $4 \leq S \leq 16$  (refer Fig. 14a). Normalized factor increases with decreasing  $d_c$  for  $4 \leq K \leq 20$  (Fig. 14b) due to enhancement in  $Y$  with reducing the constricted flow area in the middle section, under otherwise identical conditions (refer Fig. 14a). For instance,  $Y_N$  maximally enhances by 11.24% when  $d_c$  varies from 1 to 0.25 at  $S = 16$  and  $K = 8$  (refer Fig. 14b). Electroviscous correction factor ( $Y$ ) functional dependence on the dimensionless parameters ( $K, S, d_c$ ) is given below.

$$Y = A_1 + (A_2 + A_4X)X + (A_3 + A_5\gamma)\gamma + A_6X\gamma \quad (15)$$

$$\text{where } A_i = \sum_{j=1}^4 N_{ij}d_c^{(j-1)}; \quad X = K^{-1}; \quad \gamma = S^{-1}; \quad 1 \leq i \leq 6$$

where, the correlation coefficients ( $N_{ij}$ ) are statistically obtained as

$$N = \begin{bmatrix} 1.2228 & 0.7714 & -2.6779 & -1.3376 & 6.1330 & 0.0088 \\ -0.8179 & 1.5979 & 6.4765 & -2.3153 & -15.8020 & 0.1167 \\ 0.6728 & -6.3056 & -1.3392 & 12.7820 & 2.4928 & -0.1008 \\ -0.1397 & 4.0203 & -1.9083 & -8.6731 & 5.3792 & 0.0139 \end{bmatrix}^T$$

by performing the non-linear regression analysis using the DataFit (trial version) with  $(\delta_{\min}, \delta_{\max}, \delta_{\text{avg}}, R^2)$  as (-3.94%, 3.93%, -0.04%, 97.21%) for given ranges of conditions.

## 4.7. Pseudo-analytical model

The flow characteristics for electrolyte liquid flow through charged slit microfluidic device have been calculated numerically as discussed in the above sections. However, it can be calculate analytically for wide ranges of parameters and broad microfluidic applications for design aspects. Previous studies have proposed simpler analytical model to calculate the pressure drop ( $\Delta P$ ) in the symmetrically ( $S_r = 1$ ) charged device for no-slip, charge-dependent slip flow and in the asymmetrically ( $S_r \neq 1$ ) charged microfluidic device with contraction-expansion ( $d_c = 0.25$ ) cross-section [18, 20, 22, 27]. Analytically estimated pressure drop from these studies overpredicts the numerically estimated pressure drop maximally by 5 – 10%.

In this study, earlier analytical model [18, 20, 22, 27] is extended for electrolyte liquid flow through charged slit microfluidic device for variable contraction ratio ( $0.25 \leq d_c \leq 1$ ). The pressure drop ( $\Delta P$ ) for laminar steady incompressible Newtonian fully developed flow through slit microfluidic device of length ( $L$ ) for non-EVF ( $S = 0$ ) is computed by summing up the individual uniform (upstream, contraction, downstream) sections pressure drop ( $\Delta P_u$ ,  $\Delta P_c$ ,  $\Delta P_d$ ) by standard *Hagen-Poiseuille* equation and excess pressure drop ( $\Delta P_e$ ) because of sudden contraction/expansion is predicted by pressure drop through thin orifices ( $d_c \ll 1$ ) [18, 19, 22, 63]. It is expressed as follows

$$\Delta P_{00,m} = \left( \sum_{i=u,c,d} \Delta P_{00,i} \right) + \Delta P_{00,e} \quad (16)$$

where, the subscripts '00',  $u$ ,  $c$ , and  $d$  denote non-EVF ( $S = 0$  or  $K = \infty$ ) with fixed contraction ( $d_c = 0.25$ ), upstream, contraction, and downstream sections, respectively and these sections

individually represent slit microchannel of uniform cross-section. The pressure terms are expressed as follows.

$$\Delta P_{0,i} = \left( \frac{3}{Re} \right) \frac{\Delta L_i}{d_i^3}; \quad \Delta P_{0,e} = \frac{16}{\pi d_c^2 Re}; \quad \text{where} \quad d_i = \frac{W_i}{W}$$

where  $d_c$  is the contraction ratio. The lengths ( $L_u$ ,  $L_d$ , and  $L_c$ ) are scaled with  $W$  and Reynolds number ( $Re$ ) is defined in the Eq. (2).

Subsequently, Eq. (16) is extended, and generalized pressure drop for variable contraction ( $0.25 \leq d_c \leq 1$ ) in absence of electric field ( $S = 0$ ) is expressed as follows.

$$\Delta P_{0,m} = \frac{3}{Re} \left[ L_u + \frac{\alpha L_c}{d_c^3} + L_d + \frac{16\alpha}{3\pi d_c^2} \right] \quad (17)$$

The influence of contraction variation ( $0.25 \leq d_c \leq 1$ ) on the pressure drop ( $\Delta P_{00,m}$ ) is accounted by correction coefficient ( $\alpha$ , Eq. 17) and it is expressed as follows.

$$\alpha = C_1 + C_2 d_c + C_3 d_c^2 \quad (18)$$

The correlation coefficients ( $C_i$ , Eq. 18) are statistically obtained as  $C_1 = 1.022$ ,  $C_2 = -0.0635$ , and  $C_3 = -0.2148$  by performing the non-linear regression analysis with ( $\delta_{\min}$ ,  $\delta_{\max}$ ,  $\delta_{\text{avg}}$ ,  $R^2$ ) as (-0.77%, 0.68%, -0.01%, 99.99) for given ranges of conditions.

Eqs. (16) and (17) expressed a generalized simpler analytical model for the low Reynolds number ( $Re = 0.01$ ) flow of liquid through a slit microfluidic device at fixed  $d_c (= 0.25)$  and variable  $d_c$ , respectively excluding electric field ( $S = 0$ ) and it is further extended considering

both electroviscous ( $S > 0$ ) and contraction variation ( $0.25 \leq d_c \leq 1$ ) effects is given below.

$$\Delta P_m = \Gamma_{\text{evcv}} \Delta P_{0,m} = \Gamma_{\text{evcv}} \left[ \frac{3}{Re} \left( L_u + \frac{\alpha L_c}{d_c^3} + L_d + \frac{16\alpha}{3\pi d_c^2} \right) \right] \quad (19)$$

where subscript 'evcv' denotes electroviscous and contraction variation (EVCV) effects.

The influence of both contraction variation ( $0.25 \leq d_c \leq 1$ ) and electroviscous ( $S > 0$ ) effects on the pressure drop ( $\Delta P_{0,m}$ ) is accounted by correction coefficient ( $\Gamma_{\text{evcv}}$ , Eq. 19) and it is expressed as follows.

$$\Gamma_{\text{evcv}} = A_1 + (A_2 + A_4 X)X + (A_3 + A_5 \gamma)\gamma + A_6 X^{0.5} \gamma$$

where  $A_i = \sum_{j=1}^4 N_{ij} d_c^{(j-1)}$ ;  $X = K^{-1}$ ;  $\gamma = S^{-1}$ ;  $1 \leq i \leq 6$  (20)

The correlation coefficients ( $N_{ij}$ , Eq. 20) are statistically obtained as

$$N = \begin{bmatrix} 1.2444 & -0.7322 & 0.6237 & -0.153 \\ 1.0135 & 4.7458 & -9.0319 & 4.4003 \\ -2.8434 & 4.2179 & 0.6104 & -2.1758 \\ -1.4557 & -3.8409 & 14.1 & -8.8549 \\ 7.1203 & -2.7138 & -8.8752 & 6.9885 \\ -0.6105 & -7.8852 & 6.8532 & -0.9721 \end{bmatrix}$$

by performing the non-linear regression analysis with ( $\delta_{\min}$ ,  $\delta_{\max}$ ,  $\delta_{\text{avg}}$ ,  $R^2$ ) as (-4.10%, 2.90%, -0.05%, 98.60%) for given ranges of conditions.

The above discussed simple analytical model (Eqs. 17 and 19) for low Reynolds number ( $Re = 0.01$ ) electrolyte liquid flow through slit microfluidic device considering variable

contraction ( $0.25 \leq d_c \leq 1$ ) is further extended to calculate the electroviscous correction factor is expressed as follows.

$$Y_m = \frac{\Delta P_m}{\Delta P_{0,m}} \quad (21)$$

Figs. 15a and b depict parity charts for present numerical approach and simpler predictive model

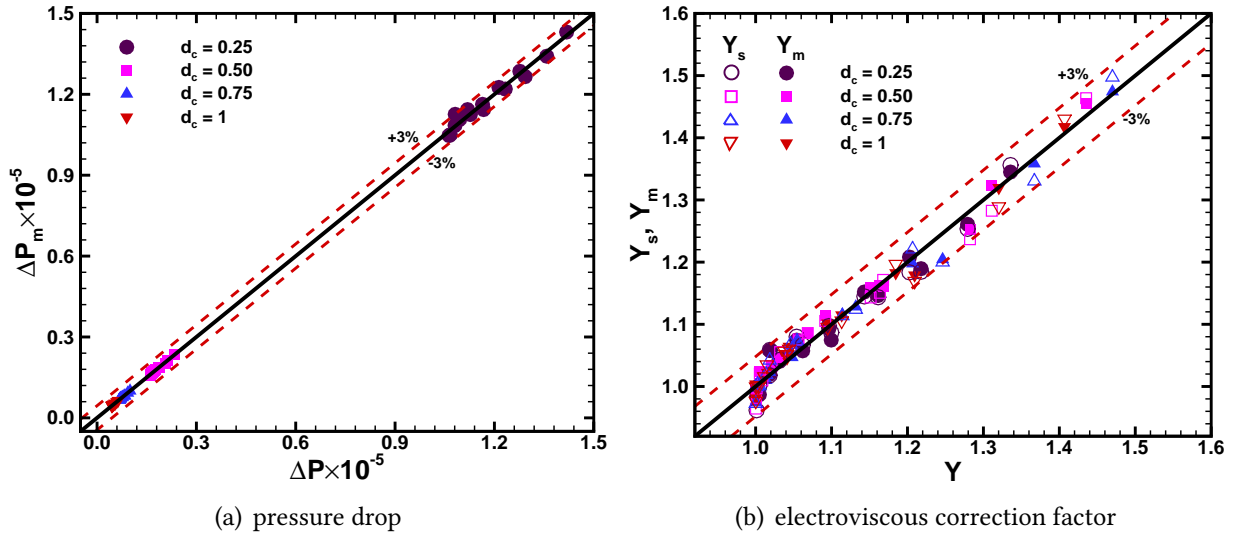


Figure 15: Parity chart for (a) numerically ( $\Delta P$ ) and mathematically ( $\Delta P_m$ , Eq. 19) obtained pressure drop, (b) numerically ( $Y$ ) and mathematically ( $Y_s$ , Eq. 15;  $Y_m$ , Eq. 21) obtained electroviscous correction factor for  $K$ ,  $S$  and  $d_c$ .

obtained pressure drop ( $\Delta P$  vs  $\Delta P_m$ ) and electroviscous correction factor ( $Y$  vs  $Y_m$ ) for  $K$ ,  $S$ , and  $d_c$ . The simple analytical model overpredicts both pressure drop and electroviscous correction factor  $\pm 3\%$  of the numerical results. The difference between numerical and predicted results is smaller with decreasing surface charge density ( $S$ ) and increasing inverse Debye length ( $K$ ) or thinning of the EDL.

## 5. CONCLUDING REMARKS

In this work, contraction variation and electroviscous effects have investigated in the symmetric (1:1) electrolyte liquid flow through charged slit microfluidic device at low Reynolds number ( $Re = 10^{-2}$ ). A finite element method (FEM) is used to solve the mathematical model consisting of Poisson's, Nernst-Planck, and Navier-Stokes equations numerically to obtain the flow fields such as total electrical potential ( $U$ ), ionic charge ( $n_{\pm}$ ), excess charge ( $n^*$ ), induced electric field strength ( $E_x$ ), velocity ( $\mathbf{V}$ ) and pressure ( $P$ ) fields for broader ranges of dimensionless governing parameters ( $2 \leq K \leq 20$ ,  $4 \leq S \leq 16$ ,  $0.25 \leq d_c \leq 1$ ).

Flow characteristics in the microfluidic device have shown complex dependency on the governing parameters ( $K$ ,  $S$ ,  $d_c$ ). Total potential and pressure drop maximally change by 1785.58% (0.2118 to 3.9929) and 2300.83% (0.0450 to 1.0815), respectively with reducing contraction  $d_c$  from 1 to 0.25, over the ranges of conditions. The electroviscous correction factor (i.e., ratio of apparent to physical viscosity) maximally increases by 11.24% (at  $K = 8$ ,  $S = 16$ ), 31.80% (at  $S = 16$ ,  $d_c = 0.75$ ), and 22.89% (at  $K = 2$ ,  $d_c = 0.5$ ) when  $d_c$  varies from 1 to 0.25 ( $0.25 \leq d_c \leq 1$ ),  $K$  changes from 20 to 2 ( $2 \leq K \leq 20$ ), and  $S$  varies from 4 to 16 ( $4 \leq S \leq 16$ ), respectively. Further, overall increment in electroviscous correction factor is noted as 46.99% (at  $K = 2$ ,  $S = 16$ ,  $d_c = 0.75$ ), relative to non-EVE ( $S = 0$ ). Thus, increment in the contraction enhances the electroviscous effects in the microfluidic devices. However, it is worth noted that maximum  $Y$  is obtained at  $d_c = 0.75$  than other  $d_c$ , for given ranges of  $2 \leq K \leq 20$  and  $4 \leq S \leq 16$ .

A simple analytical model is developed to predict the pressure drop and electroviscous correction factor for broad ranges of flow governing parameters. This analytical model results estimate



the pressure drop within  $\pm 2-3\%$  to the present numerical results. The difference between the analytical and present numerical results reduces with decreasing  $S$  and increasing  $K$  or thinning of EDL. The present numerical results enable the use of these results to design essential and reliable microfluidic devices for various microfluidic applications.

## DECLARATION OF COMPETING INTEREST

The authors declare that they have no known competing financial interests or personal relationships that could have appeared to influence the work reported in this paper.

## ACKNOWLEDGEMENTS

The authors acknowledge the infrastructural, computing resources, and software license support from the Indian Institute of Technology Roorkee. JD is thankful to the Department of Higher Education, Ministry of Education (MoE), Government of India (GoI) for the providence of research fellowship.

## NOMENCLATURE

$\mathcal{D}$	diffusivity of the positive and negative ions, assumed equal ( $\mathcal{D}_+ = \mathcal{D}_- = \mathcal{D}$ ), $\text{m}^2/\text{s}$
$d_c$	contraction ratio ( $= W_c/W$ , Eq. 1), –
$\mathcal{D}_j$	diffusivity of the ions of type $j$ , $\text{m}^2/\text{s}$
$e$	elementary charge of a proton ( $= 1.602176634 \times 10^{-19}$ ), C or A.s
$E_x$	induced electric field strength, V/m or –
$\mathbf{f}_j$	flux density of the ions of type $j$ (Eq. 11), $1/(\text{m}^2.\text{s})$
$I_c$	conduction current density (Eq. 9), $\text{A}/\text{m}^2$ or –

$I_d$	diffusion current density (Eq. 9), A/m <sup>2</sup> or –
$I_s$	streaming current density (Eq. 9), A/m <sup>2</sup> or –
$k_B$	Boltzmann constant ( $= 1.380649 \times 10^{-23}$ ), J/K
$L_c$	length of contraction section, m or –
$L_c^*$	generalized length of contraction section, m or –
$L_d$	length of downstream outlet section, m or –
$L_u$	length of upstream inlet section, m or –
$n_+$	local number density of positive ions (Eq. 8), 1/m <sup>3</sup> or –
$n_-$	local number density of negative ions (Eq. 8), 1/m <sup>3</sup> or –
$n_0$	bulk density of the ions of type j, 1/m <sup>3</sup>
$n_j$	local number density of the ions of type j, 1/m <sup>3</sup>
$n^*$	excess charge ( $= n_+ - n_-$ ), 1/m <sup>3</sup> or –
$P$	pressure, Pa or –
$T$	temperature, K
$U$	total electrical potential, V or –
$\mathbf{V}$	velocity vector, m/s or –
$\bar{V}$	average velocity of the fluid at the inlet, m/s
$V_x$	x-component of the velocity, m/s or –
$V_y$	y-component of the velocity, m/s or –
$W$	cross-sectional width of inlet and outlet sections, m
$W_c$	cross-sectional width of contraction section, m
$x$	streamwise coordinate, –
$Y$	electroviscous correction factor (Eqs. 14, 15, and 21), –
$y$	transverse coordinate, –
$z_j$	valency of the ions of type j, assumed equal ( $z_+ = z_- = z$ ), –

*Dimensionless groups*

$\beta$	liquid parameter (Eq. 2), –
$K$	inverse Debye length (Eq. 2), –
$Pe$	Peclet number ( $= Re Sc$ ) (Eq. 2), –

$Re$  Reynolds number (Eq. 2), –

$S$  surface charge density (Eq. ??), –

$Sc$  Schmidt number (Eq. 2), –

#### *Greek letters*

$\Delta P$  pressure drop (Eqs. 17 and 19), –

$\varepsilon_0$  permittivity of free space (i.e. vacuum), F/m or C/(V.m)

$\varepsilon_r$  dielectric constant (or absolute permittivity or relative permittivity) of the electrolyte liquid, –

$\lambda_D$  Debye length  $\left( = \sqrt{\frac{\varepsilon_0 \varepsilon_r k_B T}{z^2 e^2 n_0}} \right)$ , m

$\mu$  viscosity, Pa.s

$\mu_{\text{eff}}$  effective or apparent viscosity, Pa.s

$\psi$  EDL potential, V or –

$\rho$  density of fluid, kg/m<sup>3</sup>

$\rho_e$  charge density of liquid, C/m<sup>3</sup>

$\sigma$  surface charge density, C/m<sup>2</sup>

#### *Subscripts and Superscripts*

$c$  contraction

$d$  downstream

$e$  extra or excess

$m$  mathematical

$s$  statistical

$u$  upstream

0 without electroviscous effects

00 without electroviscous effects and fixed contraction ( $d_c = 0.25$ )

#### *Abbreviations*

CFD computational fluid dynamics

EDL electrical double layer

EV electroviscous

EVCV electroviscous and contraction variation

EVF electroviscous flow

FEM finite element method

PDF pressure-driven flow

## APPENDIX A. ADDITIONAL INFORMATION

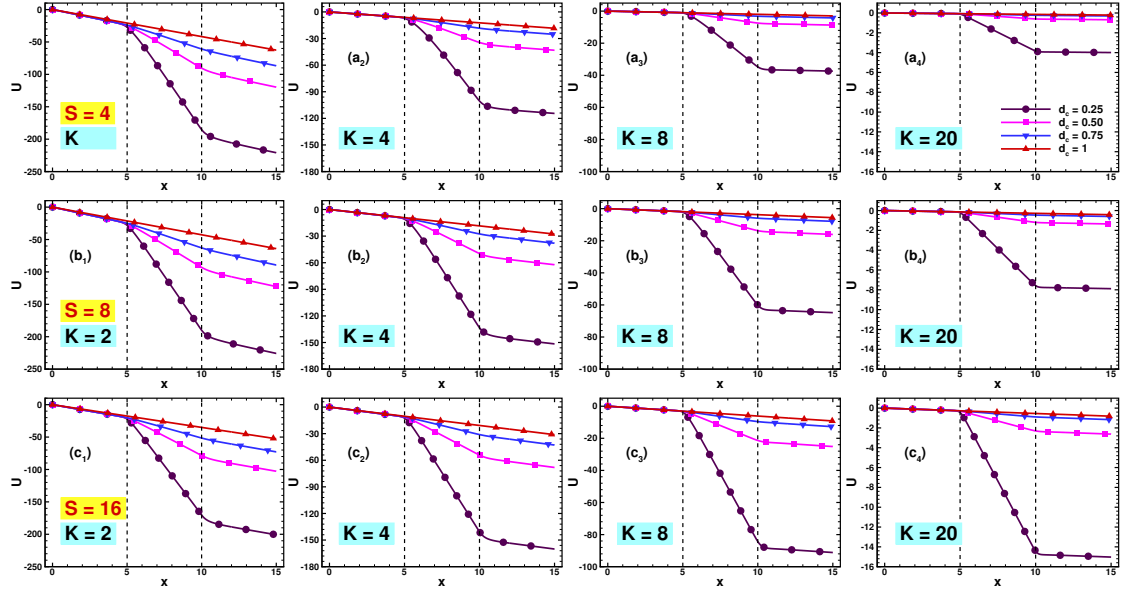


Figure A.1: Dimensionless total electrical potential ( $U$ ) distribution on the centreline of charged microfluidic device as a function of dimensionless governing parameters ( $K$ ,  $S$  and  $d_c$ ).

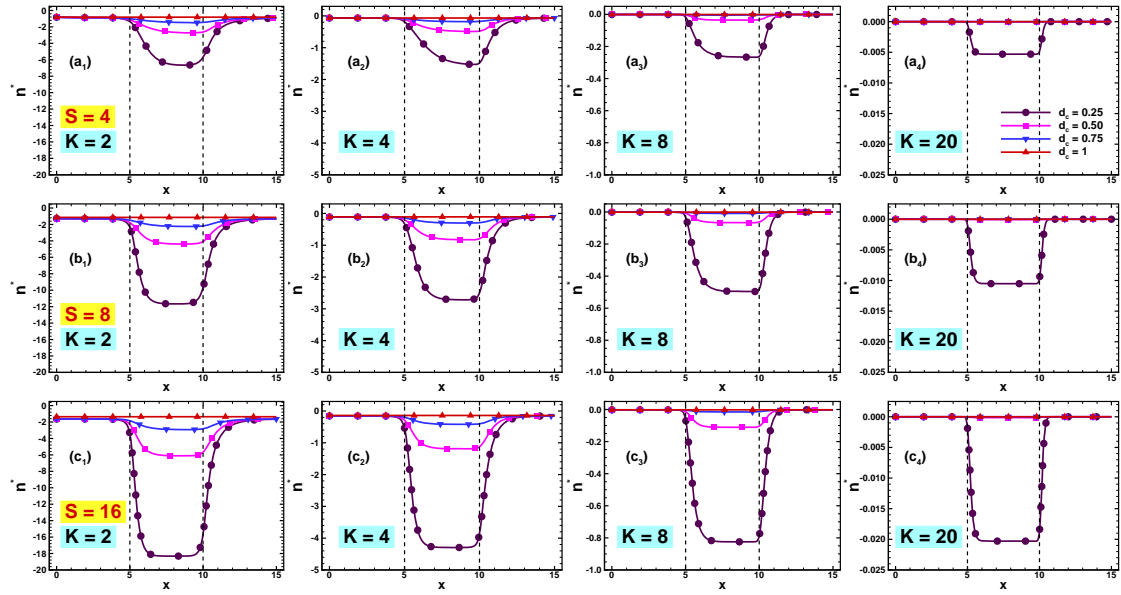


Figure A.2: Dimensionless excess charge ( $n^*$ ) distribution on the centreline of charged microfluidic device as a function of dimensionless governing parameters ( $K$ ,  $S$  and  $d_c$ ).

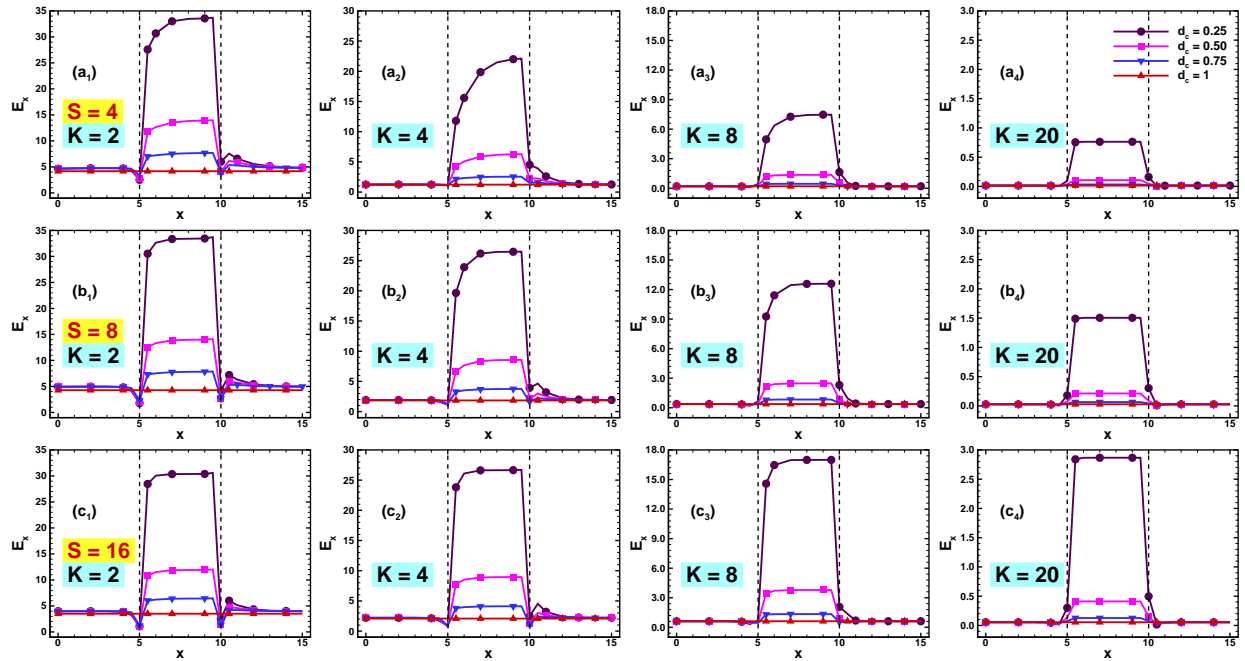


Figure A.3: Dimensionless induced electric field strength ( $E_x$ ) distribution on the centreline of charged microfluidic device as a function of dimensionless governing parameters ( $K$ ,  $S$  and  $d_c$ ).

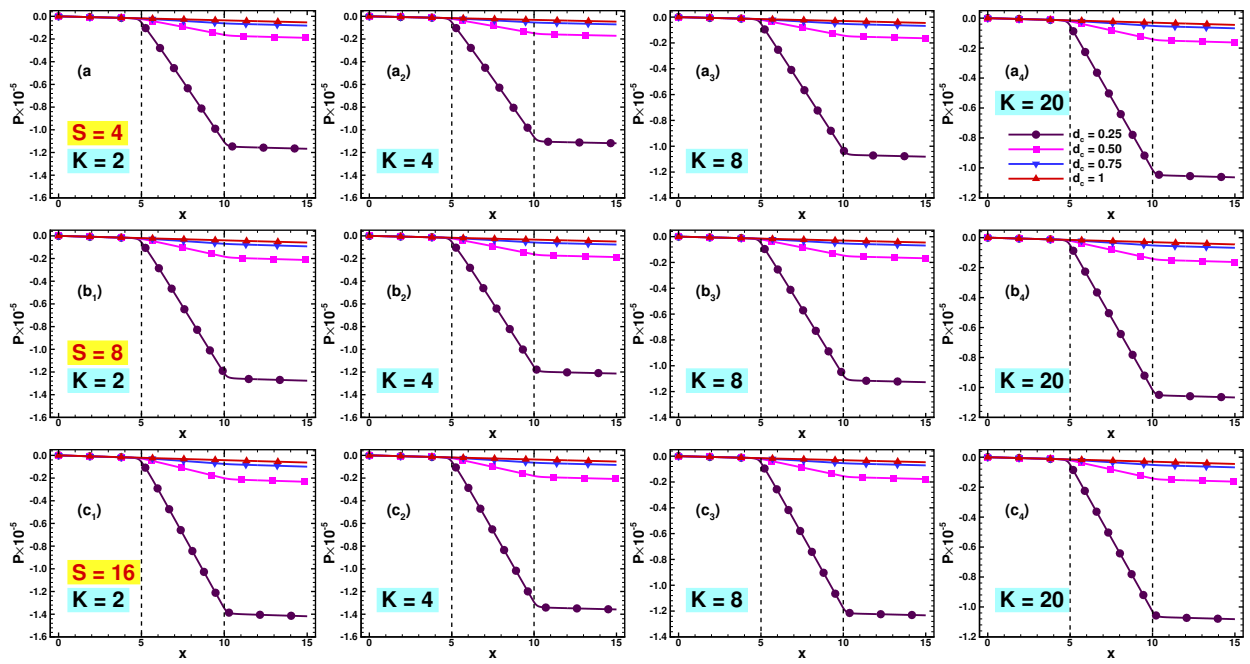


Figure A.4: Dimensionless pressure ( $P$ ) distribution on the centreline of charged microfluidic device as a function of dimensionless governing parameters ( $K$ ,  $S$  and  $d_c$ ).

## REFERENCES

- [1] A. M. Foudeh, T. F. Didar, T. Veres, M. Tabrizian, Microfluidic designs and techniques using lab-on-a-chip devices for pathogen detection for point-of-care diagnostics, *Lab on a Chip* 12 (18) (2012) 3249–3266.
- [2] B. Bruijns, A. Van Asten, R. Tiggelaar, H. Gardeniers, Microfluidic devices for forensic DNA analysis: A review, *Biosensors* 6 (3) (2016) 41.
- [3] X. J. Li, Y. Zhou, *Microfluidic Devices for Biomedical Applications*, Woodhead Publishing, 2021.
- [4] G. T. Vladislavljević, N. Khalid, M. A. Neves, T. Kuroiwa, M. Nakajima, K. Uemura, S. Ichikawa, I. Kobayashi, Industrial lab-on-a-chip: Design, applications and scale-up for drug discovery and delivery, *Advanced Drug Delivery Reviews* 65 (11-12) (2013) 1626–1663.
- [5] N.-T. Nguyen, S. A. M. Shaegh, N. Kashaninejad, D.-T. Phan, Design, fabrication and characterization of drug delivery systems based on lab-on-a-chip technology, *Advanced Drug Delivery Reviews* 65 (11-12) (2013) 1403–1419.
- [6] D. Figeys, D. Pinto, Lab-on-a-chip: a revolution in biological and medical sciences., *Analytical Chemistry* 72 (9) (2000) 330 A–335 A.
- [7] J. Wu, M. Dong, C. Rigatto, Y. Liu, F. Lin, Lab-on-chip technology for chronic disease diagnosis, *NPJ Digital Medicine* 1 (1) (2018) 1–11.
- [8] H. Xue, K. Ng, J. Wang, Performance evaluation of the recuperative heat exchanger in a miniature Joule–Thomson cooler, *Applied Thermal Engineering* 21 (18) (2001) 1829–1844.
- [9] I. Stogiannis, A. Mouza, S. Paras, Efficacy of SiO<sub>2</sub> nanofluids in a miniature plate heat exchanger with undulated surface, *International Journal of Thermal Sciences* 92 (2015) 230–238.
- [10] M. Bahiraei, S. M. Naghibzadeh, M. Jamshidmofid, Efficacy of an eco-friendly nanofluid in a miniature heat exchanger regarding to arrangement of silver nanoparticles, *Energy Conversion and Management* 144 (2017) 224–234.
- [11] M. Pan, H. Wang, Y. Zhong, T. Fang, X. Zhong, Numerical simulation of the fluid flow and heat transfer characteristics of microchannel heat exchangers with different reentrant cavities, *International Journal of*

- Numerical Methods for Heat & Fluid Flow* 29 (11) (2019) 4334–4348.
- [12] A. A. Imran, N. S. Mahmoud, H. M. Jaffal, Numerical and experimental investigation of heat transfer in liquid cooling serpentine mini-channel heat sink with different new configuration models, *Thermal Science and Engineering Progress* 6 (2018) 128–139.
- [13] A. A. Abdulqadur, H. M. Jaffal, D. S. Khudhur, Performance optimiation of a cylindrical mini-channel heat sink using hybrid straight–wavy channel, *International Journal of Thermal Sciences* 146 (2019) 106111.
- [14] H. Tan, L. Wu, M. Wang, Z. Yang, P. Du, Heat transfer improvement in microchannel heat sink by topology design and optimization for high heat flux chip cooling, *International Journal of Heat and Mass Transfer* 129 (2019) 681–689.
- [15] D. Zhuang, Y. Yang, G. Ding, X. Du, Z. Hu, Optimization of microchannel heat sink with rhombus fractal-like units for electronic chip cooling, *International Journal of Refrigeration* 116 (2020) 108–118.
- [16] R. J. Hunter, *Zeta Potential in Colloid Science: Principles and Applications*, Academic Press, 1981.
- [17] D. Li, Electro-viscous effects on pressure-driven liquid flow in microchannels, *Colloids and Surfaces A: Physicochemical and Engineering Aspects* 195 (1-3) (2001) 35–57.
- [18] M. R. Davidson, D. J. E. Harvie, Electroviscous effects in low Reynolds number liquid flow through a slit-like microfluidic contraction, *Chemical Engineering Science* 62 (16) (2007) 4229–4240.
- [19] F. Pimenta, K. Toda-Peters, A. Q. Shen, M. A. Alves, S. J. Haward, Viscous flow through microfabricated axisymmetric contraction/expansion geometries, *Experiments in Fluids* 61 (9) (2020) 1–16.
- [20] J. Dhakar, R. P. Bharti, Electroviscous effects in charge-dependent slip flow of liquid electrolytes through a charged microfluidic device, *Chemical Engineering and Processing-Process Intensification* (2022) 109041.
- [21] S. Sisavath, X. Jing, C. C. Pain, R. W. Zimmerman, Creeping flow through an axisymmetric sudden contraction or expansion, *Journal of Fluids Engineering* 124 (1) (2002) 273 – 278.
- [22] R. P. Bharti, D. J. E. Harvie, M. R. Davidson, Steady flow of ionic liquid through a cylindrical microfluidic contraction–expansion pipe: Electroviscous effects and pressure drop, *Chemical Engineering Science* 63 (14) (2008) 3593–3604.
- [23] R. P. Bharti, D. J. E. Harvie, M. R. Davidson, Electroviscous effects in steady fully developed flow of a power-law



- liquid through a cylindrical microchannel, *International Journal of Heat and Fluid Flow* 30 (4) (2009) 804–811.
- [24] M. R. Davidson, R. P. Bharti, P. Liovic, D. J. Harvie, Electroviscous effects in low Reynolds number flow through a microfluidic contraction with rectangular cross-section, in: *Proceedings of World Academy of Science, Engineering and Technology*, vol. 30, 256–260, 2008.
- [25] M. R. Davidson, R. P. Bharti, D. J. E. Harvie, Electroviscous effects in a Carreau liquid flowing through a cylindrical microfluidic contraction, *Chemical Engineering Science* 65 (23) (2010) 6259–6269.
- [26] J. Dhakar, R. P. Bharti, Slip effects in ionic liquids flow through a contraction–expansion microfluidic device, in: R. P. Bharti, K. Gangawane (Eds.), *Recent Trends in Fluid Dynamics Research*, chap. 12, Springer, 149–159, 2022.
- [27] J. Dhakar, R. P. Bharti, Electroviscous effects in pressure-driven flow of electrolyte liquid through an asymmetrically charged non-uniform microfluidic device, *Journal of the Taiwan Institute of Chemical Engineers* 153 (2023) 105230.
- [28] D. Burgreen, F. Nakache, Electrokinetic flow in ultrafine capillary slits, *Journal of Physical Chemistry* 68 (5) (1964) 1084–1091.
- [29] G. M. Mala, D. Li, C. Werner, H.-J. Jacobasch, Y. B. Ning, Flow characteristics of water through a microchannel between two parallel plates with electrokinetic effects, *International Journal of Heat and Fluid Flow* 18 (5) (1997) 489–496.
- [30] G. M. Mala, D. Li, J. D. Dale, Heat transfer and fluid flow in microchannels, *International Journal of Heat and Mass Transfer* 40 (13) (1997) 3079–3088.
- [31] M.-S. Chun, H.-W. Kwak, Electrokinetic flow and electroviscous effect in a charged slit-like microfluidic channel with nonlinear Poisson-Boltzmann field, *Korea-Australia Rheology Journal* 15 (2) (2003) 83–90.
- [32] C. L. Ren, D. Li, Electroviscous effects on pressure-driven flow of dilute electrolyte solutions in small microchannels, *Journal of Colloid and Interface Science* 274 (1) (2004) 319–330.
- [33] X. Chen, K. Toh, J. Chai, C. Yang, Developing pressure-driven liquid flow in microchannels under the electrokinetic effect, *International Journal of Engineering Science* 42 (5-6) (2004) 609–622.
- [34] L. Joly, C. Ybert, E. Trizac, L. Bocquet, Liquid friction on charged surfaces: From hydrodynamic slippage to

- electrokinetics, *The Journal of Chemical Physics* 125 (20) (2006) 204716.
- [35] X. Xuan, Streaming potential and electroviscous effect in heterogeneous microchannels, *Microfluidics and Nanofluidics* 4 (5) (2008) 457–462.
- [36] L. Wang, J. Wu, Flow behavior in microchannel made of different materials with wall slip velocity and electroviscous effects, *Acta Mechanica Sinica* 26 (1) (2010) 73–80.
- [37] J. Jamaati, H. Niazmand, M. Renksizbulut, Pressure-driven electrokinetic slip-flow in planar microchannels, *International Journal of Thermal Sciences* 49 (7) (2010) 1165–1174.
- [38] C. Zhao, C. Yang, On the competition between streaming potential effect and hydrodynamic slip effect in pressure-driven microchannel flows, *Colloids and Surfaces A: Physicochemical and Engineering Aspects* 386 (1-3) (2011) 191–194.
- [39] D. Tan, Y. Liu, Combined effects of streaming potential and wall slip on flow and heat transfer in microchannels, *International Communications in Heat and Mass Transfer* 53 (2014) 39–42.
- [40] D. Jing, B. Bhushan, Electroviscous effect on fluid drag in a microchannel with large zeta potential, *Beilstein Journal of Nanotechnology* 6 (1) (2015) 2207–2216.
- [41] M. H. Matin, W. A. Khan, Electrokinetic effects on pressure driven flow of viscoelastic fluids in nanofluidic channels with Navier slip condition, *Journal of Molecular Liquids* 215 (2016) 472–480.
- [42] D. Jing, Y. Pan, X. Wang, The non-monotonic overlapping EDL-induced electroviscous effect with surface charge-dependent slip and its size dependence, *International Journal of Heat and Mass Transfer* 113 (2017) 32–39.
- [43] M. H. Matin, Electroviscous effects on thermal transport of electrolytes in pressure driven flow through nanoslit, *International Journal of Heat and Mass Transfer* 106 (2017) 473–481.
- [44] S. I. Kim, S. J. Kim, Analysis of the electroviscous effects on pressure-driven flow in nanochannels using effective ionic concentrations, *Microfluidics and Nanofluidics* 22 (1) (2018) 12.
- [45] A. Sailaja, B. Srinivas, I. Sreedhar, Electroviscous effect of power law fluids in a slit microchannel with asymmetric wall zeta potentials, *Journal of Mechanics* 35 (4) (2019) 537–547.
- [46] X. Mo, X. Hu, Electroviscous effect on pressure driven flow and related heat transfer in microchannels with

- surface chemical reaction, *International Journal of Heat and Mass Transfer* 130 (2019) 813–820.
- [47] C. Li, Z. Liu, X. Liu, Z. Feng, X. Mo, Combined effect of surface charge and boundary slip on pressure-driven flow and convective heat transfer in nanochannels with overlapping electric double layer, *International Journal of Heat and Mass Transfer* 176 (2021) 121353.
- [48] C. Li, Z. Liu, N. Qiao, Z. Feng, Z. Q. Tian, The electroviscous effect in nanochannels with overlapping electric double layers considering the height size effect on surface charge, *Electrochimica Acta* 419 (2022) 140421.
- [49] D. Banerjee, S. Pati, P. Biswas, Analysis of electroviscous effect and heat transfer for flow of non-Newtonian fluids in a microchannel with surface charge-dependent slip at high zeta potentials, *Physics of Fluids* 34 (11) (2022) 112016.
- [50] J. Xing, Y. Liu, Combined electromagnetohydrodynamic flow in microchannels with consideration of the surface charge-dependent slip, *Physica Scripta* 98 (2) (2023) 025202.
- [51] C. Yang, D. Li, J. H. Masliyah, Modeling forced liquid convection in rectangular microchannels with electrokinetic effects, *International Journal of Heat and Mass Transfer* 41 (24) (1998) 4229–4249.
- [52] L. Ren, D. Li, W. Qu, Electro-viscous effects on liquid flow in microchannels, *Journal of Colloid and Interface Science* 233 (1) (2001) 12–22.
- [53] J.-P. Hsu, C.-Y. Kao, S. Tseng, C.-J. Chen, Electrokinetic flow through an elliptical microchannel: Effects of aspect ratio and electrical boundary conditions, *Journal of Colloid and Interface Science* 248 (1) (2002) 176–184.
- [54] C. L. Rice, R. Whitehead, Electrokinetic flow in a narrow cylindrical capillary, *Journal of Physical Chemistry* 69 (11) (1965) 4017–4024.
- [55] S. Levine, J. Marriott, G. Neale, N. Epstein, Theory of electrokinetic flow in fine cylindrical capillaries at high zeta-potentials, *Journal of Colloid and Interface Science* 52 (1) (1975) 136–149.
- [56] W. R. Bowen, F. Jenner, Electroviscous effects in charged capillaries, *Journal of Colloid and Interface Science* 173 (2) (1995) 388–395.
- [57] D. Brutin, L. Tadrist, Modeling of surface-fluid electrokinetic coupling on the laminar flow friction factor in microtubes, *Microscale Thermophysical Engineering* 9 (1) (2005) 33–48.

- [58] D. Jing, Y. Pan, Electroviscous effect and convective heat transfer of pressure-driven flow through microtubes with surface charge-dependent slip, *International Journal of Heat and Mass Transfer* 101 (2016) 648–655.
- [59] J. D. Berry, M. R. Davidson, R. P. Bharti, D. J. E. Harvie, Effect of wall permittivity on electroviscous flow through a contraction, *Biomicrofluidics* 5 (4) (2011) 044102.
- [60] D. J. Harvie, C. J. Biscombe, M. R. Davidson, Microfluidic circuit analysis I: Ion current relationships for thin slits and pipes, *Journal of Colloid and Interface Science* 365 (1) (2012) 1–15.
- [61] M. R. Davidson, J. D. Berry, R. Pillai, D. J. Harvie, Numerical simulation of two-fluid flow of electrolyte solution with charged deforming interfaces, *Applied Mathematical Modelling* 40 (3) (2016) 1989–2001.
- [62] L. Zhongwu, M. Rahul Prasanna, L. Yuhao, Y. Yun-Chiao, Z. Sidi, Z. Yuliang, C. Yunfei, B. Daniel, N. Aleksandr, Breakdown of the Nernst–Einstein relation in carbon nanotube porins, *Nature Nanotechnology* 18 (2) (2023) 177 – 183.
- [63] S. Sisavath, X. Jing, C. C. Pain, R. W. Zimmerman, Creeping flow through an axisymmetric sudden contraction or expansion, *Journal of Fluids Engineering* 124 (1) (2002) 273–278.